Progress In Electromagnetics Research B, Vol. 75, 149–173, 2017

Eliminate Crosstalk Using Symmetry in MIMO Arrays of Inductive Antennas: An Introduction to Pie-Chart Antennas

Jean-Philippe Douarville-Blaise[1, *], David Pouhè[2], and Junji Hirai[1]

Abstract—We present a topology of MIMO arrays of inductive antennas exhibiting inherent high crosstalk cancellation capabilities. A single layer PCB is etched into a 3-channels array of emitting/receiving antennas. Once coupled with another similar 3-channels emitter/receiver, we measured an Adjacent Channel Rejection Ratio (ACRR) as high as 70 dB from 150 Hz to 150 kHz. Another primitive device made out of copper wires wound around PVC tubes to form a 2-channels "non-contact slip-ring" exhibited 22 dB to 47 dB of ACRR up to 15 MHz. In this paper we introduce the underlying theoretical model behind the crosstalk suppression capabilities of those so-called "*Pie-Chart antennas*": an extension of the mutual inductance compensation method to higher number of channels using symmetries. We detail the simple iterative building process of those antennas, illustrate it with numerical analysis and evaluate there effectiveness via real experiments on the 3-channels PCB array and the 2-channels rotary array up to the limit of our test setup. The Pie-Chart design is primarily intended as an alternative solution to costly electronic filters or cumbersome EM shields in wireless AND wired applications, but not exclusively.

1. INTRODUCTION

What if we could increase data rate while reducing bit error rate, development time and production cost of wired and wireless signal transmissions systems? In this paper we introduce our piece of answer to those concerns in the form of a simple concept: the Pie-Chart antenna.

Suppose a bunch of sensors mounted on the blades of a wind turbine. How to supply power to those sensors and monitor them in real-time? This type of problem is commonly addressed using batteries, slip rings and/or wireless technologies such as W-LAN, Bluetooth, ZigBee, etc. [1, 2]. In paper [3], Bieler et al. propose a very simple and compact solution: power and information are transmitted by induction on two physically distinct channels. The beauty of his solution lies in that, however the power coil is almost wound into the data coil, crosstalk is almost null. When dealing with crosstalk, such a solution can significantly reduce the need for magnetic guides, shielding or electronic components [11], hence potentially lowering weight, size, complexity, cost and increasing reliability of transmission systems.

The Pie-Chart antenna concept is an extension of T. Bieler's solution to higher number of channels. It is similarly based on the method of mutual inductance cancellation using symmetries. This concept is indeed extendable well beyond the limited frame of electromagnetism (acoustic, vibrations and any wave-signals in general). Yet, in this introductory paper we will focus on the very limited case of filamentary antenna working in the magneto-static domain. A more complete electromagnetic model along with its implications as well as a variety of concrete applications of this concept will be presented later in two dedicated papers entitled "*Eliminate Crosstalk using Symmetry in MIMO Arrays of Inductive Antenna: Miscellaneous Properties of Pie-Chart Antennas.*" and "*Eliminate Crosstalk using Symmetry in MIMO Arrays of Inductive Antenna: Miscellaneous Applications of Pie-Chart Antennas.*".

Received 12 February 2017, Accepted 28 April 2017, Scheduled 7 June 2017

* Corresponding author: Jean-Philippe Douarville-Blaise (pier.jp.douarvil@gmail.com).

[1] School of Electrical and Electronics Engineering, Mie University, Japan. [2] School of Engineering, Reutlingen University, Germany.

Fig. 1 can also be seen as the cross-section of a 4 channels Pie-Chart cable, or that of 4 channels Pie-Chart non-contact linear sliding connection: plus and minus signs would then indicate the location of the conductors and the orientation of their current along the $\hat{\mathbf{k}}$ axis while the oriented paths would indicate the corresponding magnetic field's orientation. In the case of a cable however, the 1st channel is incomplete (only one wire represented by the white plus sign). A concentric cylindrical conductive sleeve braided around the whole cable would provide an ideal return line for this channel as it will also provide additional shielding to the cable.

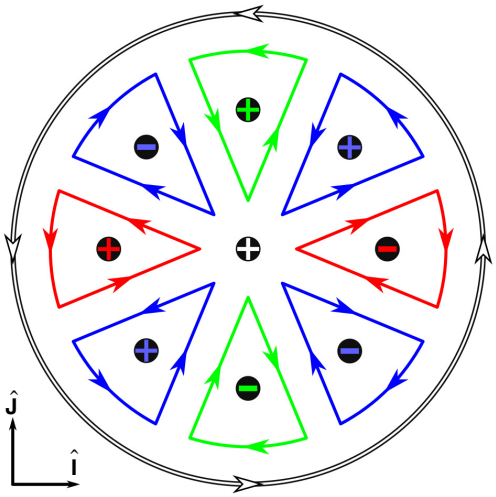

Figure 1. This Pie-Chart array looks like... a pie. This figure can be seen as the conductor layout of a flat (e.g., tracks of a PCB) 4 channels Pie-Chart inductive emitter (or receiver). Red and green oriented paths would respectively represent the 2nd and 3rd channels emitter's (receiver's) track. They both are 2nd order Pie-Chart arrays. Blue oriented path would represent the 4th channel emitter's (receiver's) track. It is a 3rd order Pie-Chart array. White oriented outer circle would represent the 1st channel emitter's (receiver's) track. It is a special 1st order Pie-Chart antenna: it has infinite number of plane of anti-symmetry. Plus and minus signs indicate the magnetic field's orientation along the $\hat{\mathbf{k}}$ axis given the correspondingly colored current paths.

2. THEORETICAL ANALYSIS

In the following we consider a working medium of linear homogeneous isotropic electromagnetic properties filling an infinite tridimensional euclidean space. The medium has a magnetic permeability $\mu = \mu_0\mu_r$, where μ_r is its relative permeability and $\mu_0 = 4\pi \times 10^7\,\mathrm{T\,m\,A^{-1}}$. The default Cartesian frame of reference is defined as $(O;\hat{\mathbf{i}},\hat{\mathbf{j}},\hat{\mathbf{k}})$.

2.1. Definitions

2.1.1. Reflexive Symmetry Function

Suppose a plane $Q_{\vec{n},\vec{A}}$ normal to a vector $\vec{n} = n_x\hat{\mathbf{i}} + n_y\hat{\mathbf{j}} + n_z\hat{\mathbf{k}} \neq \vec{0}$ and including a point A located by $\vec{A} = \overrightarrow{OA} = A_x\hat{\mathbf{i}} + A_y\hat{\mathbf{j}} + A_z\hat{\mathbf{k}}$. The function $Z(\vec{P},\vec{n},\vec{A})$ which associates to any point P its orthogonal symmetric $\underset{\vec{n},\vec{A}}{\widetilde{P}}$ by the plane $Q_{\vec{n},\vec{A}}$ (Fig. 2) is defined by:

$$\begin{aligned} Z : (\mathbb{R}^3,\mathbb{R}^3,\mathbb{R}^3) &\rightarrow \mathbb{R}^3 \\ (\vec{P},\vec{n},\vec{A}) &\mapsto \tilde{P} = \frac{1}{\vec{n}^2}(2[\mathbf{B}]\vec{A} + [\mathbf{C}]\vec{P}) \end{aligned} \tag{1}$$

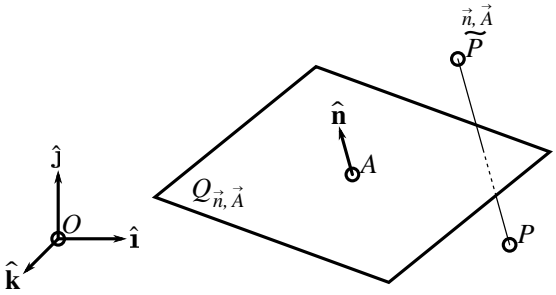

Figure 2. $\widetilde{P}^{\vec{n},\vec{A}}$ symmetric of P through $Q_{\vec{n},\vec{A}}$.

where $[\mathbf{B}] = \vec{n}^T \times \vec{n}$ ($\vec{n}$ is a row vector) and $[\mathbf{C}] = \vec{n}^2 \times [\mathbf{I}]_3 - 2[\mathbf{B}]$ ($[\mathbf{I}]_3$ is the 3×3 unit matrix). Then:

- Z is an isometry of the euclidean space.
- For any given vectors $\vec{U}$ and $\vec{V}$:

$$\widetilde{\vec{U}}^{\vec{n},\vec{A}} - \widetilde{\vec{V}}^{\vec{n},\vec{A}} = \widetilde{\vec{U} - \vec{V}}^{\vec{n},\vec{A}} \tag{2}$$

$$\widetilde{\vec{U}}^{\vec{n},\vec{0}} \times \widetilde{\vec{V}}^{\vec{n},\vec{0}} = -\widetilde{\vec{U} \times \vec{V}}^{\vec{n},\vec{0}} \tag{3}$$

$$\widetilde{\vec{U}}^{\vec{n},\vec{0}} \cdot \widetilde{\vec{V}}^{\vec{n},\vec{0}} = \vec{U} \cdot \vec{V} \tag{4}$$

2.1.2. Antenna

The term antenna refers to any closed oriented 3D path. We model it as a parametric curve:

$$\begin{array}{rcl} \zeta :]a,b[& \to & \mathbb{R}^3 \\ t & \mapsto & \vec{\zeta}(t) = \begin{pmatrix} x(t) \\ y(t) \\ z(t) \end{pmatrix}_{\hat{\mathbf{i}},\hat{\mathbf{j}},\hat{\mathbf{k}}} \end{array} \tag{5}$$

differentiable on $]a,b[$ where $\lim_{t\to a} \vec{\zeta}(t) = \lim_{t\to b} \vec{\zeta}(t)$ are respectively the positive and negative antenna's terminals.

The electric current $\vec{i}(t)$ through ζ is defined at each point $\vec{\zeta}(t)$ by:

$$\vec{i}(t) = i(t) \cdot \frac{\vec{\zeta}'(t)}{\|\vec{\zeta}'(t)\|} \tag{6}$$

where $i(t) \in \mathbb{R}$ is the current intensity and $\vec{\zeta}'(t)/\|\vec{\zeta}'(t)\|$ is the curve's orientation vector at $\vec{\zeta}(t)$.

2.1.3. Array

An array [of antennas] refers to a tuple of n antennas $\vec{\zeta}_i$, where $n \in \mathbb{N}$, all linked to a common signal S via transfer functions of their electric current $\vec{i}_i(t,S)$ or electric potential $V_i(t,S)$ at each point $\vec{\zeta}_i(t)$.

2.1.4. Magneto-Static Approximation

In this paper, we consider that, at any instant, the current's wavelength is long enough to be consider of uniform intensity along each individual filamentary antenna it flows in. Therefore the mutual inductance

$M_{i,j}$ between two antennas ζ_i and ζ_j can be determined using the following Neumann Equation [4]:

$$M_{i,j} = \frac{\mu}{4\pi} \cdot \oint_{\zeta_i} \oint_{\zeta_j} \frac{\overrightarrow{dl}_i \cdot \overrightarrow{dl}_j}{\|\vec{r}_{i,j}\|} \tag{7}$$

where $\overrightarrow{dl}_i = \overrightarrow{\zeta}'_i(t_i)dt_i$, $\overrightarrow{dl}_j = \overrightarrow{\zeta}'_j(t_j)dt_j$ and $\vec{r}_{i,j} = \overrightarrow{\zeta}_j(t_j) - \overrightarrow{\zeta}_i(t_i)$. Given that $\overrightarrow{dl}_i$ and $\overrightarrow{dl}_j$ are independent, this equation leads to $M_{i,j} = M_{j,i}$.

2.2. Model

In this subsection parameters $\vec{n}$ and $\vec{A}$ are constants. Readers may refer to Fig. 3 of Subsection 3.3 for visual reference.

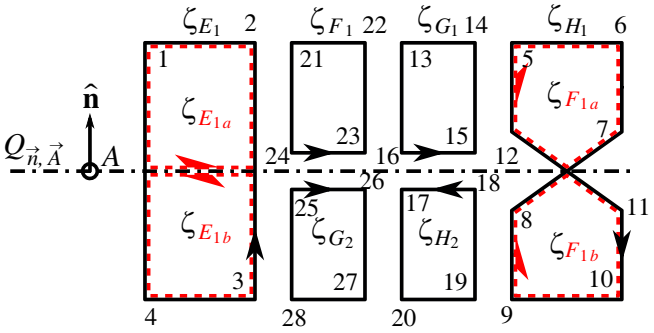

Pt	x	y	z
1	0	3.5	0
4	0	0	0
7	6.5	2.5	4.5
10	6.5	0	4.5
13	3.5	3.5	0
16	3.5	2	0
19	4.5	0	3
22	3	3.5	3
25	2	1.5	0
28	2	0	0

Pt	x	y	z
2	1.5	3.5	4.5
5	5	3.5	0
8	5	1	0
11	6.5	1	4.5
14	4.5	3.5	3
17	3.5	1.5	0
20	3.5	0	0
23	3	2	3
26	3	1.5	3
A	-1	1.75	0

Pt	x	y	z
3	1.5	0	4.5
6	6.5	3.5	4.5
9	5	0	0
12	5	2.5	0
15	4.5	2	3
18	4.5	1.5	3
21	2	3.5	0
24	2	2	0
27	3	0	3
$\hat{\mathbf{n}}$	0	1	0

Figure 3. Arbitrary symmetric and anti-symmetric arrays of antennas. Arrows indicate the antenna's orientation. 3D coordinates of the points 1 to 28 are expressed in meters. Notice that ζ_{E_1} and ζ_F are homeomorphic to their symmetric/anti-symmetric. For a better visualization of the situation, they can be seen as the serial combination of the manifold red dashed paths $\zeta_{E_{1a}}$ and $\zeta_{E_{1b}}$, respectively $\zeta_{F_{1a}}$ and $\zeta_{F_{1b}}$.

2.2.1. Emitters Geometry

ζ_E is an emitting array of m geometrically distinct antennas admitting $Q_{\vec{n},\vec{A}}$ as a plane of anti-symmetry of ζ_E (symmetric paths but reverse symmetric orientation). That is to say, the elements ζ_{E_i} of ζ_E are constrained in shape and orientation in the manner:

$$\begin{array}{rcl} \forall i \leq m, i \in \mathbb{N}^* \ : \ \exists! j / \ \ \zeta_{E_i} : \ ]-e,e[& \rightarrow & \mathbb{R}^3 \\ \alpha & \mapsto & \left| \begin{array}{l} \vec{\zeta}_{E_i}(\alpha) = \overset{\vec{n},\vec{A}}{\widetilde{\zeta}}_{E_j}(-\alpha) \\ \vec{\zeta}'_{E_i}(\alpha) = -\overset{\vec{n},\vec{0}}{\widetilde{\zeta}'}_{E_j}(-\alpha) \end{array} \right. \end{array} \tag{8}$$

For conciseness, we will use the notation $\zeta_{E_i} = \overset{\vec{n},\vec{A}}{\rightleftharpoons} \zeta_{E_j}$ to represent this relation of reflexive *anti-symmetry* by the plane $Q_{\vec{n},\vec{A}}$ between the two individual antennas ζ_{E_i} and ζ_{E_j}. By extension, we will use this same notation $\zeta_E = \overset{\vec{n},\vec{A}}{\rightleftharpoons} \zeta_E$ to represent the reflexive anti-symmetry relation between two arrays ζ_E and $\overset{\vec{n},\vec{A}}{\rightleftharpoons} \zeta_E$.

ζ_F is an emitting antenna array of n geometrically distinct antennas admitting $Q_{\vec{n},\vec{A}}$ as a plane of symmetry of ζ_F. That is to say, the elements ζ_{F_i} of ζ_F are constrained in shape and orientation in the

manner:

$$\begin{array}{rcl} \forall i \leq n, i \in \mathbb{N}^* \ : \ \exists! j / \ \ \zeta_{F_i} : \ ]-f, f[& \rightarrow & \mathbb{R}^3 \\ \alpha & \mapsto & \left| \begin{array}{l} \vec{\zeta}_{F_i}(\alpha) = \overset{\vec{n},\vec{A}}{\widetilde{\zeta}}_{F_j}(-\alpha) \\ \vec{\zeta}'_{F_i}(\alpha) = \overset{\vec{n},\vec{0}}{\widetilde{\zeta}'}_{F_j}(-\alpha) \end{array} \right. \end{array} \tag{9}$$

For conciseness, we will use the notation $\zeta_{F_i} = \overset{\vec{n},\vec{A}}{\Leftrightarrow}_{F_j}$ to represent this relation of reflexive symmetry by the plane $Q_{\vec{n},\vec{A}}$ between the two individual antennas ζ_{F_i} and ζ_{F_j}. By extension, we will use this same notation $\zeta_F = \overset{\vec{n},\vec{A}}{\Leftrightarrow}_F$ to represent the reflexive symmetry relation between two arrays ζ_F and $\overset{\vec{n},\vec{A}}{\Leftrightarrow}_F$.

2.2.2. Receivers Geometry

ζ_G and ζ_H are receiving arrays of respectively o and p geometrically distinct antennas defined on $]-g, g[$ and $]-h, h[$ as:

$$\zeta_G = \overset{\vec{n},\vec{A}}{\rightleftharpoons}_G \tag{10}$$

$$\zeta_H = \overset{\vec{n},\vec{A}}{\Leftarrow}_H \tag{11}$$

2.2.3. Mutual Inductance

Considering the above described antenna configuration, we can determine the mutual inductance between each couple of antennas of ζ_E and ζ_F as:
$\forall (i,k) \leq (m,n), (i,k) \in \mathbb{N}^{2*}$:

$$\begin{aligned} M_{E_i,F_k} &= \frac{\mu}{4\pi} \cdot \int_{-e}^{e} \int_{-f}^{f} \frac{-\overset{\vec{n},\vec{A}}{\widetilde{\zeta}'}_{E_j}(-\alpha) \cdot \overset{\vec{n},\vec{A}}{\widetilde{\zeta}'}_{F_l}(-\beta)}{\| \overset{\vec{n},\vec{A}}{\widetilde{\zeta}}_{F_l}(-\beta) - \overset{\vec{n},\vec{A}}{\widetilde{\zeta}}_{E_j}(-\alpha) \|} \, d\beta \, d\alpha \\ &= \frac{\mu}{4\pi} \cdot \int_{e}^{-e} \int_{f}^{-f} \frac{-\overset{\vec{n},\vec{A}}{\widetilde{\zeta}'}_{E_j}(\gamma) \cdot \overset{\vec{n},\vec{A}}{\widetilde{\zeta}'}_{F_l}(\delta)}{\| \overset{\vec{n},\vec{A}}{\widetilde{\zeta}}_{F_l}(\delta) - \overset{\vec{n},\vec{A}}{\widetilde{\zeta}}_{E_j}(\gamma) \|} \, d\gamma \, d\delta = -M_{E_j,F_l} \end{aligned} \tag{12}$$

where $\zeta_{E_i} = \overset{\vec{n},\vec{A}}{\rightleftharpoons}_{E_j}$ and $\zeta_{F_k} = \overset{\vec{n},\vec{A}}{\Leftarrow}_{F_l}$. Similarly, we can establish that:
$(i,k) \in \mathbb{N}^{2*}$:

$$\forall (i,k) \leq (m,o) : M_{E_i,G_k} = M_{E_j,G_l} \tag{13}$$

$$\forall (i,k) \leq (m,p) : M_{E_i,H_k} = -M_{E_j,H_l} \tag{14}$$

$$\forall (i,k) \leq (n,o) : M_{F_i,G_k} = -M_{F_j,G_l} \tag{15}$$

$$\forall (i,k) \leq (n,p) : M_{F_i,H_k} = M_{F_j,H_l} \tag{16}$$

$$\forall (i,k) \leq (o,p) : M_{G_i,H_k} = -M_{G_j,H_l} \tag{17}$$

$i \in \mathbb{N}^*$:

$$\forall i \leq m : M_{E_i,E_i} = M_{E_j,E_j} \tag{18}$$

$$\forall i \leq n : M_{F_i,F_i} = M_{F_j,F_j} \tag{19}$$

$$\forall i \leq o : M_{G_i,G_i} = M_{G_j,G_j} \tag{20}$$

$$\forall i \leq p : M_{H_i,H_i} = M_{H_j,H_j} \tag{21}$$

where $\zeta_{G_i} = \overset{\vec{n},\vec{A}}{\rightleftharpoons} \zeta_{G_j}$ and $\zeta_{H_k} = \overset{\vec{n},\vec{A}}{\rightleftharpoons} \zeta_{H_l}$.

Given the above relations, the fact that the EMF ΔV_i across the terminals of an inductor ζ_i induced by the current of uniform intensity i_j flowing through an antenna ζ_j can be determined at any instant t using Faraday's law as follows

$$\Delta V_i = M_{ij} \frac{d\ i_j}{dt}, \tag{22}$$

and reminding that every antenna's current or electromotive force (EMF) of a given array is linked to one common signal via transfer functions (cf. Section 2.1.3), one can think of ways to combine the antennas so that the output signal $S_G(t)$ of ζ_G depends only on the input signal $S_E(t)$ of ζ_E and the output signal $S_H(t)$ of ζ_H only on the input signal $S_F(t)$ of ζ_F. In the following subsection, we present the simplest antenna combination which meets those requirements.

2.2.4. Mutual Inductance Compensation Layout

We combine each emitting antenna ζ_{E_i} of ζ_E with its anti-symmetric ζ_{E_j} such as at each instant t:

$$\forall i \in \mathbb{N}^*, \quad i \leq m : \zeta_{E_i} \cup \zeta_{E_j} \Leftrightarrow \frac{di_{E_i}}{dt} = \frac{di_{E_j}}{dt} = \mathcal{F}_{E_i}(S_E(t)) \tag{23}$$

where $\mathcal{F}_{E_i}$ is an arbitrary transfer function. Similarly, we combine each emitting antenna ζ_{F_i} of ζ_F with its symmetric ζ_{F_j} such as at each instant t:

$$\forall i \in \mathbb{N}^*, \quad i \leq n : \zeta_{F_i} \cup \zeta_{F_j} \Leftrightarrow \frac{d\ i_{F_i}}{dt} = \frac{d\ i_{F_j}}{dt} = \mathcal{F}_{F_i}(S_F(t)) \tag{24}$$

where $\mathcal{F}_{F_i}$ is an arbitrary transfer function.

We now combine each receiving antenna ζ_{G_i} of ζ_G with its anti-symmetric ζ_{G_j} such as at each instant t:

$$\forall i \in \mathbb{N}^*, \quad i \leq o : \zeta_{G_i} \cup \zeta_{G_j} \Leftrightarrow S_G(t) = \mathcal{F}_G(\mathcal{G}_1, \ldots, \mathcal{G}_i, \ldots, \mathcal{G}_o) \tag{25}$$

where $\mathcal{F}_G$ is an arbitrary transfer function, $\mathcal{G}_i = \Delta V_{G_i} + \Delta V_{G_j}$, and ΔV_{G_i} is the EMF across the terminals of ζ_{G_i}. Similarly, we combine each receiving antenna ζ_{H_i} of ζ_H with its symmetric ζ_{H_j} such as at each instant t:

$$\forall i \in \mathbb{N}^*, \quad i \leq p : \zeta_{H_i} \cup \zeta_{H_j} \Leftrightarrow S_H(t) = \mathcal{F}_H(\mathcal{H}_1, \ldots, \mathcal{H}_i, \ldots, \mathcal{H}_p) \tag{26}$$

where $\mathcal{F}_H$ is an arbitrary transfer function, $\mathcal{H}_i = \Delta V_{H_i} + \Delta V_{H_j}$, and ΔV_{H_i} is the EMF across the terminals of ζ_{H_i}.

In practice, this combination can be achieved simply by connecting each ζ_{E_i} in series† with ζ_{E_j}, each ζ_{F_i} in series† with ζ_{F_j}, each ζ_{G_i} in series† with ζ_{G_j} and each ζ_{H_i} in series† with ζ_{H_j}.

2.2.5. Proof

Given $\zeta_{E_i} = \overset{\vec{n},\vec{A}}{\rightleftharpoons} \zeta_{E_j}$, $\zeta_{F_k} = \overset{\vec{n},\vec{A}}{\rightleftharpoons} \zeta_{F_l}$, $\zeta_{G_i} = \overset{\vec{n},\vec{A}}{\rightleftharpoons} \zeta_{G_j}$, $\zeta_{H_k} = \overset{\vec{n},\vec{A}}{\rightleftharpoons} \zeta_{H_l}$, and based on relations (13), (14) and (22), every $\mathcal{G}_i$ can be expressed as a function of the input signals $S_E(t)$ and $S_F(t)$ so that:
$\forall i \in \mathbb{N}^{2*}, i \leq o$:

$$\begin{aligned} \mathcal{G}_i \ = \ & \Delta V_{G_i} + \Delta V_{G_j} + \left(\sum_{k=1}^{m} M_{G_i,E_k} \cdot \mathcal{F}_{E_k}(S_E) + M_{G_j,E_l} \cdot \mathcal{F}_{E_l}(S_E) \right) \\ & + \left(\sum_{k=1}^{n} M_{G_i,F_k} \cdot \mathcal{F}_{F_k}(S_F) + M_{G_j,F_l} \cdot \mathcal{F}_{F_l}(S_F) \right) \end{aligned}$$

† In theory, parallel connection should work as well. In practice, the slight differences in antenna's Equivalent Series Resistance would require a balancing circuit to achieve perfect crosstalk cancellation. Parallel connection may thus be a more flexible combination method yet more complicated to put in application. Of course, parallel and series connections are not the only possibilities...

$$\mathcal{G}_i \;=\; 2\sum_{k=1}^{m} M_{G_i,E_k}\cdot\mathcal{F}_{E_k}(S_E) \tag{27}$$

Thus the output signal $S_G(t)$ of the anti-symmetric antenna array ζ_G is independent of the input signal $S_F(t)$.

Similarly, based on relations (15) and (16), every $\mathcal{H}_i$ can be expressed as a function of the input signals $S_E(t)$ and $S_F(t)$ so that:

$$\forall i\in\mathbb{N}^{2*},\quad i\le p:\quad \mathcal{H}_i = 2\sum_{k=1}^{n} M_{H_i,F_k}\cdot\mathcal{F}_{F_k}(S_F(t)) \tag{28}$$

Thus the output signal $S_H(t)$ of the symmetric antenna array ζ_H is independent of the input signal $S_E(t)$.

2.2.6. Partial Conclusion

Given a set of parameters $\vec{n}$ and $\vec{A}$, we show that a channel $\{S_G, S_E\}$ of $Q_{\vec{n},\vec{A}}$ anti-symmetric emitting (ζ_E) and receiving (ζ_G) arrays can, in practice, be made independent of another channel $\{S_H, S_F\}$ of $Q_{\vec{n},\vec{A}}$ symmetric emitting (ζ_F) and receiving (ζ_H) arrays using elementary combination method (series connection, parallel connection, ...).

Although the conclusion drawn here is a special case encompassed by the maximal ratio combining technique (MRC) [5, 6], the approach presented here is original in that it eases a lot of the design process of multichannel antenna design, as we will illustrate it in the following example. More importantly, this is a fundamental element of the Pie-Chart antenna concept presented in the next section.

2.3. Example: Serial Layout

Let's consider the emitting arrays $\zeta_E = \zeta_{E_1}$ and $\zeta_F = \zeta_{F_1}$ and the receiving arrays $\zeta_G = \zeta_{G_1} \cup \zeta_{G_2}$ and $\zeta_H = \zeta_{H_1} \cup \zeta_{H_2}$ illustrated on Fig. 3. They are connected in serial to their input/output signal as illustrated on Fig. 4. Paths are made of isotropic homogenous conductive material of 5 mm radius circular cross section. ζ_E and ζ_G are $Q_{\vec{n},\vec{A}}$ anti-symmetric arrays, and ζ_F and ζ_H are $Q_{\vec{n},\vec{A}}$ symmetric ones. The conveniently built *matrix of inductance* [12], numerically evaluated using the Neumann Equation (7), is provided in the table associated with Fig. 4.

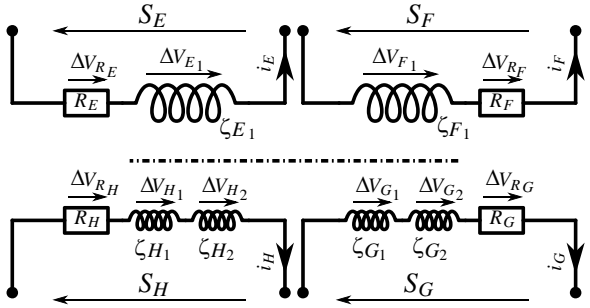

(a)

(μH)	$M_{E_{1,j}}$	$M_{F_{1,j}}$	$M_{G_{1,j}}$	$M_{G_{2,j}}$	$M_{H_{1,j}}$	$M_{H_{2,j}}$
M_{i,E_1}	20.10	0.000	0.183	0.183	0.441	-0.441
M_{i,F_1}	0.000	27.21	0.398	-0.398	0.066	0.066
M_{i,G_1}	0.183	0.398	10.11	-0.335	0.423	-0.018
M_{i,G_2}	0.183	-0.398	-0.335	10.11	0.018	-0.423
M_{i,H_1}	0.441	0.066	0.423	0.018	10.11	0.335
M_{i,H_2}	-0.441	0.066	-0.018	-0.423	0.335	10.11

(b)

Figure 4. (a) Electric circuit of the simple 2 channels inductive transmission device presented Fig. 3 and (b) the associated inductance matrix numerically evaluated. In this example, antennas ζ_{H_1} and ζ_{H_2} of the ζ_H array are combined in a serial fashion. Same goes for the antennas of the ζ_G array.

$S_E(t)$, $S_F(t)$, $S_G(t)$ and $S_H(t)$ are measured (receiver) or imposed (emitter) time-dependent EMF signals. Each signal can be expressed as a function of the others. For example:

$$\begin{aligned} S_E(t) \;=\; \Delta V_{R_E} + \Delta V_{E_1} &= i_E\cdot R_E + M_{E,E}\cdot\frac{d\,i_E(t)}{dt} + M_{E,F}\cdot\frac{d\,i_F(t)}{dt} \\ &+(M_{E,G_1}+M_{E,G_2})\cdot\frac{d\,i_G(t)}{dt} + (M_{E,H_1}+M_{E,H_2})\cdot\frac{d\,i_H(t)}{dt} \end{aligned} \tag{29}$$

Repeating this process for every antenna and given the inductance presented in Figure 4, expressions obtained for each signal are reduced to:

$$S_E(t) = i_E \cdot R_E + M_{E,E} \cdot \frac{d\ i_E}{dt} + (M_{E,G_1} + M_{E,G_2}) \cdot \frac{d\ i_G}{dt} \tag{30}$$

$$S_F(t) = i_F \cdot R_F + M_{F,F} \cdot \frac{d\ i_E}{dt} + (M_{F,H_1} + M_{F,H_2}) \cdot \frac{d\ i_H}{dt} \tag{31}$$

$$S_G(t) = i_G \cdot R_G + (M_{G_1,G_1} + M_{G_2,G_2}) \cdot \frac{d\ i_G}{dt} + (M_{G_1,E} + M_{G_2,E}) \cdot \frac{d\ i_E}{dt} \tag{32}$$

$$S_H(t) = i_H \cdot R_H + (M_{H_1,H_1} + M_{H_2,H_2}) \cdot \frac{d\ i_H}{dt} + (M_{H_1,F} + M_{H_2,F}) \cdot \frac{d\ i_F}{dt} \tag{33}$$

The above studied system is equivalent to an inductive transmission device having two independent channels: the "anti-symmetric" channel $Ch1 = \{\zeta_E, \zeta_G\}$ and the "symmetric" channel $Ch2 = \{\zeta_F, \zeta_H\}$.

3. APPLICATION: PIE-CHART ANTENNA

3.1. Iterative Building Process

Let's consider a plane $Q_{\vec{n},\vec{A}}$ and a vector $\vec{n}_0$ perpendicular to $\vec{n}$. We recursively construct any vector $\vec{n}_i$ parallel to $Q_{\vec{n},\vec{A}}$ so that $\hat{\mathbf{n}}_{i+1}$ is the vector resulting from the rotation of $\hat{\mathbf{n}}_i$ around the $(O:\vec{n})$ axis by an angle $\theta_{i+1} = \frac{\pi}{2^{i+1}}$. Hence $\vec{n}_{i+1}$ satisfies:

$$\hat{\mathbf{n}}_{i+1} = [\mathbf{R}]^{\hat{\mathbf{n}}}_{\theta_{i+1}} \times \hat{\mathbf{n}}_i \tag{34}$$

where $\hat{\mathbf{n}} = \frac{\vec{n}}{\|\vec{n}\|}$ and $[\mathbf{R}]^{\hat{\mathbf{n}}}_{\theta_{i+1}}$ is the rotation matrix:

$$[\mathbf{R}]^{\hat{\mathbf{n}}}_{\theta_{i+1}} = \begin{bmatrix} n_x^2(1-C)+C & n_x n_y(1-C)-n_z S & n_x n_z(1-C)+n_y S \\ n_x n_y(1-C)+n_z S & n_y^2(1-C)+C & n_y n_z(1-C)-n_x S \\ n_x n_z(1-C)-n_y S & n_y n_z(1-C)+n_x S & n_z^2(1-C)+C \end{bmatrix} \tag{35}$$

where $C = \cos(\theta_{i+1})$ and $S = \sin(\theta_{i+1})$. In our case, this is equivalent to:

$$\forall i \in \mathbb{N}, \left| \begin{array}{l} \vec{n}_i \neq \vec{0} \\ \hat{\mathbf{n}} \cdot \hat{\mathbf{n}}_0 = 0 \\ \hat{\mathbf{n}}_i \times \hat{\mathbf{n}}_{i+1} = -\sin(\theta_{i+1})\hat{\mathbf{n}} \\ \hat{\mathbf{n}}_i \cdot \hat{\mathbf{n}}_{i+1} = \cos(\theta_{i+1}) \end{array} \right. \tag{36}$$

Let's consider an arbitrary elemental array ξ_X. We construct an m order Pie-Chart array ζ_X^m by recursively applying the symmetry function Z as follows (Fig. 5):

$$\forall m \in \mathbb{N}^*, \forall i < m, i \in \mathbb{N}^* : \left| \begin{array}{l} \zeta^m_{X(0)} = \xi_X \\ \zeta^m_{X(i)} = \zeta^m_{X(i-1)} \cup \overrightarrow{\overrightarrow{\zeta^m_{X(i-1)}}}^{\vec{n}_{i-1},\vec{A}} \\ \zeta^m_X = \zeta^m_{X(m)} = \zeta^m_{X(m-1)} \cup \overrightarrow{\overrightarrow{\zeta^m_{X(m-1)}}}^{\vec{n}_{m-1},\vec{A}} \end{array} \right. \tag{37}$$

3.2. Proof of the Crosstalk Cancellation

- Suppose that $Q_{\vec{n}_i,\vec{A}}$ is the median plane between $Q_{\vec{n}_{i-1},\vec{A}}$ and $Q_{\vec{n}_0,\vec{A}}$ such as $-\vec{n}_0 = \overbrace{\vec{n}_{i-1}}^{\vec{n}_i,\vec{0}}$. Then based on (36) we deduce the following:

$$\left| \begin{array}{l} \hat{\mathbf{n}}_i \times \hat{\mathbf{n}}_0 = -\sin(\theta_i)\hat{\mathbf{n}} \\ \hat{\mathbf{n}}_i \cdot \hat{\mathbf{n}}_0 = \cos(\theta_i) \end{array} \right. \tag{38}$$

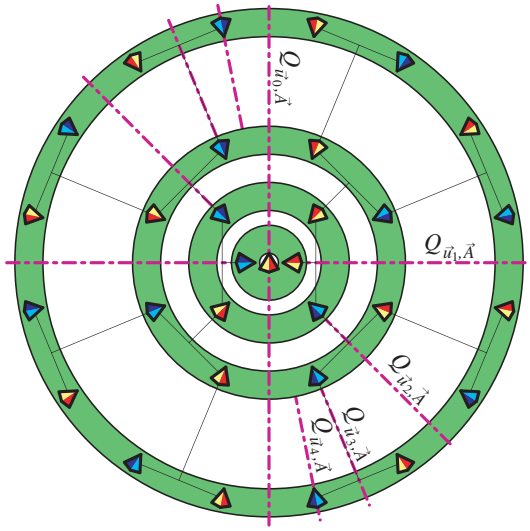

Figure 5. This radial fractal tree is an intuitive way to visualize the geometric building process of any n order Pie-Chart array. Reading starts at the center with the geometry of a 1st order Pie-Chart antenna, result of the union of a red triangle with its yellow anti-symmetric one about the $Q_{\vec{u}_0,\vec{A}}$ plane (point A is the center of the figure). Progressing on the first green ring (the smallest one), the geometry of a 2nd order array is composed of two antennas, result of the union of a red triangle and its blue symmetric about the $Q_{\vec{u}_0,\vec{A}}$ plane with their yellow and cyan anti-symmetric one about the $Q_{\vec{u}_1,\vec{A}}$ plane. And so on and so forth. Therefore, antennas on the most outer green ring can be combined into a 5th order Pie-Chart array. In practice, red/yellow figures are combined with the blue/cyan one so that current flowing through red/yellow figures flows in the opposite direction of that flowing through blue/cyan ones.

which is equivalent to:

$$\hat{\mathbf{n}}_0 = [\mathbf{R}]^{\hat{\mathbf{n}}}_{\theta_i} \times \hat{\mathbf{n}}_i \tag{39}$$

Taking notice that $\theta_{i+1} = \theta_i/2$ and remembering that $\hat{\mathbf{n}}_{i+1} = [\mathbf{R}]^{\hat{\mathbf{n}}}_{\theta_{i+1}} \times \hat{\mathbf{n}}_i$, we can deduce that $\hat{\mathbf{n}}_0 = [\mathbf{R}]^{\hat{\mathbf{n}}}_{\theta_i/2} \times ([\mathbf{R}]^{\hat{\mathbf{n}}}_{\theta_i/2} \times \hat{\mathbf{n}}_i) = [\mathbf{R}]^{\hat{\mathbf{n}}}_{\theta_{i+1}} \times \hat{\mathbf{n}}_{i+1}$. Therefore $Q_{\vec{n}_{i+1},\vec{A}}$ is the median plane between $Q_{\vec{n}_i,\vec{A}}$ and $Q_{\vec{n}_0,\vec{A}}$ such as $-\hat{\mathbf{n}}_0 = Z(\hat{\mathbf{n}}_i, \vec{n}_{i+1}, \vec{0})$.

- Based on (36) we know that $\hat{\mathbf{n}}_1 = [\mathbf{R}]^{\hat{\mathbf{n}}}_{\pi/2} \times \hat{\mathbf{n}}_0$, thus giving $-\hat{\mathbf{n}}_0 = [\mathbf{R}]^{\hat{\mathbf{n}}}_{\pi/2} \times \hat{\mathbf{n}}_1$. This is equivalent to saying that $Q_{\vec{n}_1,\vec{A}}$ is the median plane between $Q_{\vec{n}_0,\vec{A}}$ and $Q_{\vec{n}_0,\vec{A}}$ such as $-\hat{\mathbf{n}}_0 = Z(\hat{\mathbf{n}}_i, \vec{n}_{i+1}, \vec{0})$.

We can thus deduce that the last building plane of symmetry $Q_{\vec{n}_i,\vec{A}}$ of a Pie-Chart array is the median plane between $Q_{\vec{n}_{i-1},\vec{A}}$ and $Q_{\vec{n}_0,\vec{A}}$ such as $-\vec{n}_0 = Z(\vec{n}_{i-1}, \vec{n}_i, \vec{0})$.

Let's consider a body Ω_a mirror symmetric about two planes $Q_{\vec{n}_a,\vec{A}}$ and $Q_{\vec{n}_b,\vec{A}}$, and the body Ω_b defined by $\Omega_b = Z(\Omega_a, \vec{n}_c, \vec{A})$. Given that Z is an isometry of the euclidean space, we can conclude that Ω_b is mirror symmetric about the two planes $Z(Q_{\vec{n}_a,\vec{A}}, \vec{n}_c, \vec{A})$ and $Z(Q_{\vec{n}_b,\vec{A}}, \vec{n}_c, \vec{A})$.

Let's set $\vec{n}_c$ so that $Q_{\vec{n}_c,\vec{A}}$ is a median plane between $Q_{\vec{n}_a,\vec{A}}$ and $Q_{\vec{n}_b,\vec{A}}$. This means either $\hat{\mathbf{n}}_a = \overset{\vec{n}_c,\vec{0}}{\widetilde{\hat{\mathbf{n}}}}_b$ or $-\hat{\mathbf{n}}_a = \overset{\vec{n}_c,\vec{0}}{\widetilde{\hat{\mathbf{n}}}}_b$, thus resulting in:

$$\overset{\vec{n}_c,\vec{A}}{\widetilde{Q}}_{\vec{n}_a,\vec{A}} = Q_{\vec{n}_b,\vec{A}} \tag{40}$$

Indeed Ω_b stays mirror symmetric about the planes $Q_{\vec{n}_a,\vec{A}}$ and $Q_{\vec{n}_b,\vec{A}}$. Applying this result to oriented

paths, we can conclude that:

$$\zeta_m = \overleftarrow{\zeta}_m^{\vec{n}_{m-2},\vec{A}} = \overleftarrow{\zeta}_m^{\vec{n}_0,\vec{A}} = \overrightarrow{\zeta}_m^{\vec{n}_{m-1},\vec{A}} \tag{41}$$

This same statement also means that ζ_m admits $\widetilde{Q}_{\vec{n}_{m-1},\vec{A}}^{\vec{n}_{m-2},\vec{A}}$ as a plane of symmetry, as well as $Z(\widetilde{Q}_{\vec{n}_{m-1},\vec{A}}^{\vec{n}_{m-2},\vec{A}}, \widetilde{n}_{m-1}^{\vec{n}_{m-1},\vec{A}}, \vec{A})$, etc. Indeed symmetry planes of ζ_m are defined at a rotation $[\mathbf{R}]_{i\theta_{m-2}}^{\hat{\mathbf{n}}}$ of $Q_{\vec{n}_{m-2}}$, and antisymmetry planes at a rotation $[\mathbf{R}]_{i\theta_{m-2}}^{\hat{\mathbf{n}}}$ of $Q_{\vec{n}_{m-1}}$. Remembering that $\theta_{i+1} = \theta_i/2$, then $\forall i \in [1; m]$, $Q_{\vec{n}_{m-i},\vec{A}}$ is a plane of antisymmetry of ζ_m, which allows us to say:

Any m order Pie-Chart *array* ζ_m *is decoupled with any lower order* Pie-Chart *array sharing the same building parameters* $\vec{A}$, $\hat{\mathbf{n}}$ *and* $\hat{\mathbf{n}}_0$.

4. EXPERIMENTS

In the following section we present two of the experiments that we conduct to evaluate the applicability of the above theoretical model.

4.1. Three-Channels PCB Pie-Chart Array

The use of symmetry to reduce inductive crosstalk is a well-known technique [8]. However, up to current literature, this technique alone seems effective up to a maximum of 2 independent channels per axis (i.e., a maximum of 6 channels in a 3D space). In the following experiments, we measure how effective is the proposed *Pie-Chart* antenna concept to overcome this limit of 2 independent channels per axis.

4.1.1. Design and Manufacture

For speed and accuracy reasons, we decided to make the antennas by the mean of PCB etching. Insulation was ensured by a layer of about 0.1 mm thick rubber. We designed the antennas based on the following requirements:

- at least 3 coplanar channels, because 2 coplanar channels case is part of common knowledge, well documented and used in various applications.

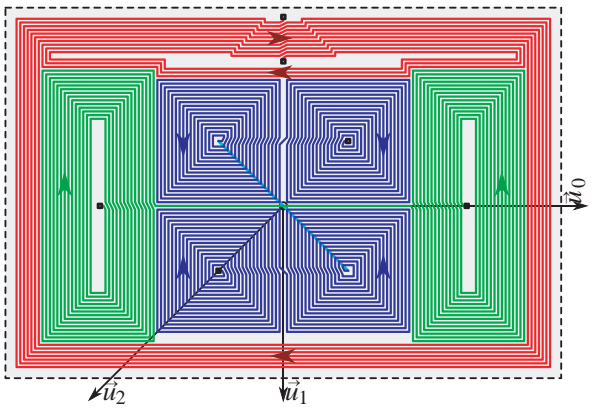

Figure 6. Tracks of the experimental PCB Pie-Chart array. 1st channel is composed of the 1st order red Pie-Chart antenna, 2nd channel is composed of the 2nd order green Pie-Chart antenna and the 3rd channel is composed of the 3rd order blue Pie-Chart antenna. Colored arrows indicate the orientation of the current inside the corresponding antenna. Vector $\vec{u}_0$, $\vec{u}_1$ and $\vec{u}_2$ are the normals of the construction planes $Q_{\vec{n}_0,\vec{A}}$ to $Q_{\vec{n}_2,\vec{A}}$. Small black squares are the antenna's terminals. Cyan line represents a link on the rear side of the PCB. Black dashed rectangle is the 150×100 mm outer limit of the PCB.

- self-inductance of every antennas must be close in order to lower the probability that the observed crosstalk attenuation is due to a difference of channel's pass-band frequency.
- given the characteristics of the used power supply ($50\,\Omega \pm 10\,\mathrm{V}$, up to 15 MHz sinusoidal waveform generator), antenna's self-inductance and electrical length must be chosen so that antennas are exploitable at frequencies lower than 15 MHz ($\simeq 20\,\mathrm{m}$ long wavelength).

Therefore, we needed a means to evaluate the inductance matrix of the system while designing the antennas. For this purpose, we wrote a rudimentary computer program (GNU Octave function) which returns the mutual inductance between any pair of arbitrary geometry antennas based on Neumann Equation (7). The final circuit shown in Fig. 6 was etched on two standard 35 µm copper plated $150 \times 100\,\mathrm{mm}$ large 1.6 mm thick glass Fiber Reinforced Epoxy boards and thinly-coated with rubber as illustrated in Fig. 7.

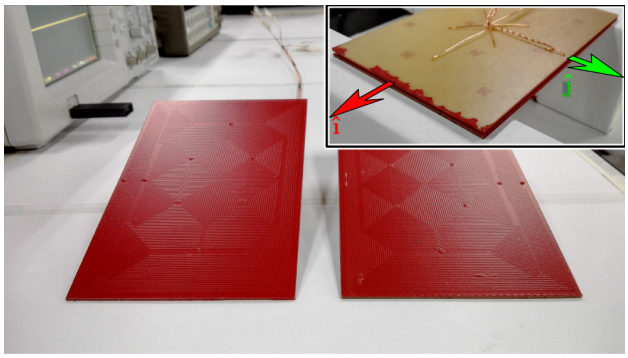

(a)

(µH)	$M_{B_1,j}$	$M_{B_2,j}$	$M_{B_3,j}$	$M_{T_1,j}$	$M_{T_2,j}$	$M_{T_3,j}$
M_{i,B_1}	13.95	0.000	0.010	12.24	0.000	0.009
M_{i,B_2}	0.000	14.13	0.003	0.000	11.98	0.004
M_{i,B_3}	0.010	0.003	14.01	0.009	0.003	11.82
M_{i,T_1}	12.24	0.000	0.009	13.95	0.000	0.010
M_{i,T_2}	0.000	11.98	0.003	0.000	14.13	0.003
M_{i,T_3}	0.009	0.004	11.82	0.010	0.003	14.01

(b)

Figure 7. (a) Photograph of the experimental 3 channels PCB type Pie-Chart array and (b) the associated inductance matrix numerically evaluated. Circuit tracks presented Fig. 6 were etched on two $150 \times 100\,\mathrm{mm}$ boards. Those PCB were then coated with a thin layer of colored rubber (red surface). Unit vectors $\hat{\mathbf{i}}$ of the X axis and $\hat{\mathbf{j}}$ of the Y axis are indicated on the top right corner image in testing configuration (i.e., one PCB flipped upside down on top of the other PCB about the Y axis).

4.1.2. Numerical Results

We consider a stack of the above presented two tri-channel arrays: one PCB is put up-side-down on top of the other and separated by a distance $h = 0.5\,\mathrm{mm}$ as shown at the top right corner of the photograph in Fig. 7. The numerically evaluated inductance matrix is given in the table of Fig. 7 given that ζ_{Bi} is the ith channel of the bottom PCB array, and ζ_{Ti} is the ith channel of the top PCB array.

The highlighted main diagonal shows that the self-inductance of each antenna is close to 14 µH. Lightly highlighted second diagonals shows that each co-channel's mutual inductance, about 12 µH, is close to antennas' self-inductance. Given formula (42) in [9], we can thus expect a minimum co-channel magnetic coupling factor $\min(k_{co}) = k_{B3,T3} = 84\%$.

$$\forall (i,j) \in \mathbb{N} : k_{i,j} = \sqrt{\frac{M_{i,j}^2}{M_{i,i} \times M_{j,j}}} \tag{42}$$

In comparison, the evaluated cross-channel's mutual inductances are not higher than 10 nH. Therefore, we can expect a maximum cross-channel magnetic coupling factor of $\max(k_{cross}) = k_{B1,B3} = 7.2 \times 10^{-2}\%$. In this configuration, assuming that the transmission of power is approximately proportional to k^2 [10], this corresponds to an expected minimal Adjacent Channel Rejection Ratio (ACRR, selectivity or signal to noise power ratio) $\min(\mathcal{S}_{i,j}) = \mathcal{S}_{B3,T2} \simeq 60\,\mathrm{dB}$ given[‡]:

$$\mathcal{S}_{i,j} = \min\left(20\log_{10}\left(\frac{k_{i1,i2}}{k_{i1,j}}\right)\right) \tag{43}$$

[‡] Based on Eq. (42), $M_{i,j} = M_{j,i}$ implies $k_{i,j} = k_{j,i}$; however, regarding Eq. (43), this does NOT imply that $\mathcal{S}_{i,j} = \mathcal{S}_{j,i}$.

where antennas ζ_{i1} and ζ_{i2} are two different antennas of the channel i, and ζ_j is an antenna of the channel j. Notice that this equation leads to $\mathcal{S}_{i,j} \propto (M_{j,j}/M_{i,i})^{1/2}$. From a crosstalk reduction stand point, this means that a given multichannel inductive system would generally benefit from designing higher power channels with proportionally higher self-inductance than lower power channels.

The same evaluation procedure was repeated in different configurations. Fig. 8 illustrates the expected evolution of the minimum ACRR between channels functions of the PCB misalignment (translation only) along the x, y and z axes.

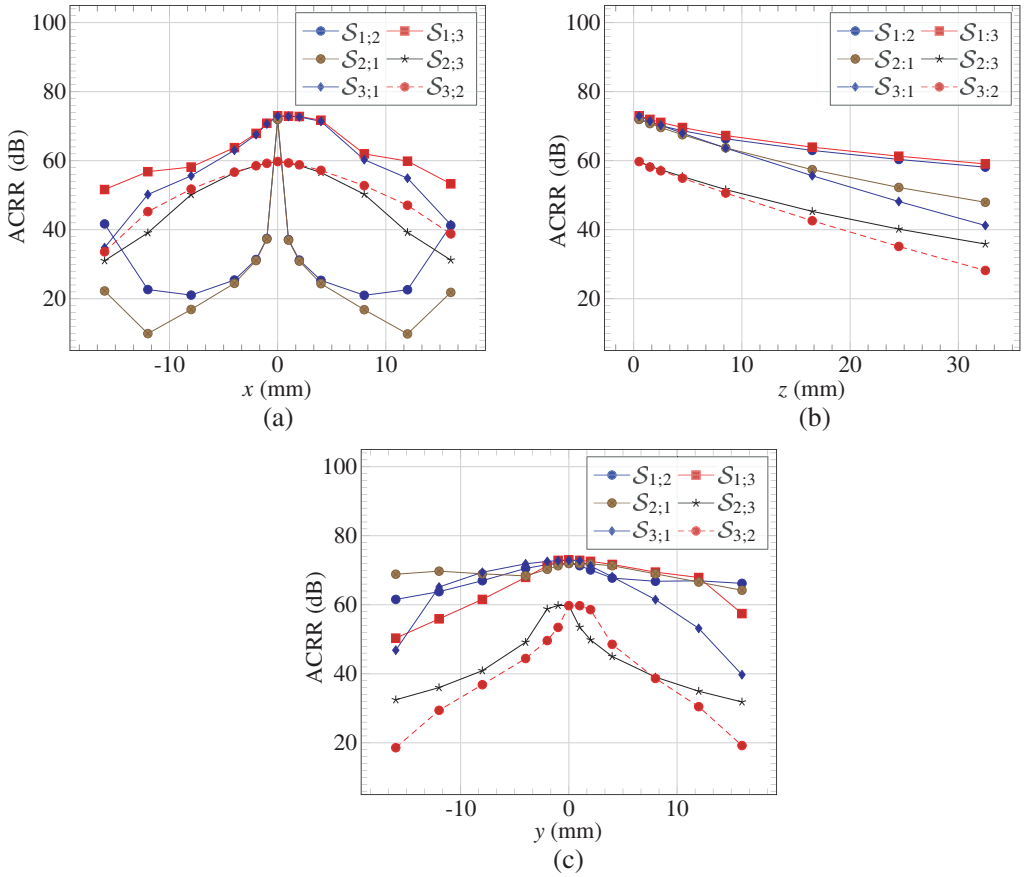

Figure 8. (a) Numerically evaluated impact of the PCB array misalignment along the x, (c) y and (b) z axes on the Adjacent Channel Rejection Ratio (ACRR).

4.1.3. Experimental Setup

We would like to experimentally determine the ACRR and the mutual inductance matrix of the system at position $(0, 0, 0.5)_{O;\hat{\mathbf{i}},\hat{\mathbf{j}},\hat{\mathbf{k}}}$ (no x, y misalignment, 0.5 mm gap).

An antenna can be configured on the fly as emitter (connected to power supply) or receiver (disconnected to power supply) thanks to the routing circuit shown in Fig. 9. Resistor R_i represents the Equivalent Series Resistance (ESR) of the antenna ζ_i. Their value are given in Table A1 of Appendix A.

Given the circuit presented in Fig. 9 and assuming that components properties are not significantly altered over the 150 Hz to 15 MHz frequency range, we can deduce the relation:

$$\begin{aligned}\Delta V_{B1} &= \Delta\delta\gamma_{B1} - R_{B1}\frac{294.4\Delta\beta\alpha - 314.4\Delta\delta\gamma_{B1}}{5888} \\ &= \Delta\delta\gamma_{B1} - R_{B1}\left(\frac{\Delta\beta\alpha}{314.4} - \frac{\Delta\delta\gamma_{B1}}{294.4}\right)\end{aligned}$$

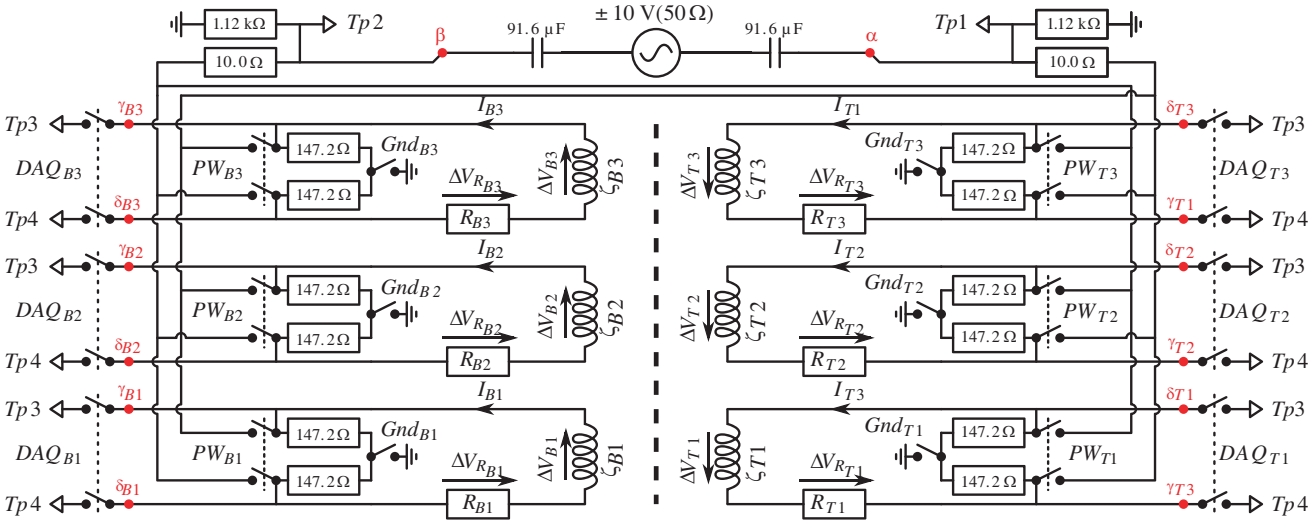

Figure 9. Routing circuit for experimental evaluation of up to 6 antenna system's inductance matrix. Signal supplied by the AC generator through 91.6 µF ceramic coupling capacitors is balanced with a pair of 1.12 kΩ resistors. It is then routed to only one emitting antenna ζ_i by closing the switches PW_i (configuration XP_i). Probed points $\{\alpha, \beta\}$ are connected to oscilloscope's 1st and 2nd inputs ($Tp1$ and $Tp2$). Probed points $\{\gamma_{B1}, \delta_{B1}\}$ to $\{\gamma_{T3}, \delta_{T3}\}$ are pairwise routable to the 3rd and 4th inputs of the oscilloscope ($Tp3$ and $Tp4$) via the switches DAQ_{B1} to DAQ_{T3}. A complete data set consists of a record of $\{\alpha, \beta, \gamma_{B1}, \delta_{B1}\}$ to $\{\alpha, \beta, \gamma_{T3}, \delta_{T3}\}$ for each configuration XP_i (6 configurations). For safety reasons and measurement consistency, given a configuration XP_i, when a signal $\Delta\gamma_j\delta_j$ $(j \neq i)$ is being measured, the switch Gnd_j is closed to balance the signal (Gnd switches are otherwise open). All represented ground points are oscilloscope's ground (independent from generator's ground). 1.12 kΩ, 10.0 Ω and 147.2 Ω resistors are thin film carbon resistors. $\Delta\alpha\beta$ is the time reference signal of each $\{\alpha, \beta, \gamma_x, \delta_x\}$ record.

$$= \sum M_{i,B1} \frac{d\, I_i}{dt} \tag{44}$$

where $\Delta\delta\gamma_{B1}$ is the electric potential difference $\gamma_{B1} - \delta_{B1}$ and $\Delta\beta\alpha$ the difference $\alpha - \beta$. This assumes that ζ_{B1} is in emitter mode. When ζ_{B1} is in receiver mode, we simply consider that $\Delta\beta\alpha = \Delta\delta\gamma_{B1}$ in Equation (44). Same goes for the five other antennas. Hence, by recording the electric potential $\{\alpha, \beta, \gamma_{B1}, \delta_{B1}\}$ to $\{\alpha, \beta, \gamma_{T3}, \delta_{T3}\}$ for 6 independent emitter/receiver configurations, namely configuration XP_{B1} to XP_{T3}, we can deduce the relations (45) and (46):

$$5888 \times [\mathbf{\Delta\gamma\delta}] - [\mathbf{R}] \times (294.4[\mathbf{\Delta\alpha\beta}] - 314.4[\mathbf{\Delta\gamma\delta}]) = [\mathbf{M}] \times \frac{d\,(294.4[\mathbf{\Delta\alpha\beta}] - 314.4[\mathbf{\Delta\gamma\delta}])}{dt} \tag{45}$$

$$\begin{aligned}
&\overset{XP_{B1}}{\downarrow} \qquad \overset{XP_{T3}}{\downarrow} \\
&5888 \begin{bmatrix} \Delta\gamma\delta_{B1} & \cdots & \Delta\gamma\delta_{T3} \\ \vdots & & \vdots \\ \Delta\gamma\delta_{T3} & & \Delta\gamma\delta_{T3} \end{bmatrix} - \begin{bmatrix} R_{B1} & & 0 \\ & \ddots & \\ 0 & & R_{T3} \end{bmatrix} \\
&\times \left(294.4 \begin{bmatrix} \Delta\alpha\beta & \cdots & \Delta\gamma\delta_{B1} \\ \vdots & \ddots & \vdots \\ \Delta\gamma\delta_{T3} & & \Delta\alpha\beta \end{bmatrix} - 314.4 \begin{bmatrix} \Delta\gamma\delta_{B1} & \cdots & \Delta\gamma\delta_{B1} \\ \vdots & & \vdots \\ \Delta\gamma\delta_{T3} & & \Delta\gamma\delta_{T3} \end{bmatrix} \right) \\
&= \begin{bmatrix} M_{B1,B1} & \cdots & M_{T3,B1} \\ \vdots & \ddots & \\ M_{B1,T3} & & M_{T3,T3} \end{bmatrix} \times \frac{d}{dt} \left(294.4 \begin{bmatrix} \Delta\alpha\beta & \cdots & \Delta\gamma\delta_{B1} \\ \vdots & \ddots & \vdots \\ \Delta\gamma\delta_{T3} & & \Delta\alpha\beta \end{bmatrix} - 314.4 \begin{bmatrix} \Delta\gamma\delta_{B1} & \cdots & \Delta\gamma\delta_{B1} \\ \vdots & & \vdots \\ \Delta\gamma\delta_{T3} & & \Delta\gamma\delta_{T3} \end{bmatrix} \right)
\end{aligned}$$

$$[\mathbf{M}] = (5888 \times [\boldsymbol{\Delta\gamma\delta}] - [\mathbf{R}] \times (294.4[\boldsymbol{\Delta\alpha\beta}] - 314.4[\boldsymbol{\Delta\gamma\delta}])) \times \left[\frac{d\ (294.4[\boldsymbol{\Delta\alpha\beta}] - 314.4[\boldsymbol{\Delta\gamma\delta}])}{dt}\right]^{-1} \quad (46)$$

In practice, configuration XP_i consisted in setting only the antenna ζ_i as an emitter and the five others set as receivers. This minimizes the risk of non-reversibility of the matrix $d(294.4[\boldsymbol{\Delta\alpha\beta}] - 314.4[\boldsymbol{\Delta\gamma\delta}])/dt$.

Measurement points Tp_1 to Tp_4 were connected to the 1 MΩ inputs of a 4 channels oscilloscope (ref: Agilent 2024A) via 1.2 m unterminated crocodile clip ended 50 Ω coaxial cable, as can be seen in Fig. 10. All four coaxial cables were twisted in one strand between the measurement points and the oscilloscope inputs to reduce ground loops. Measurements were performed inside an anechoic chamber at 20°C.

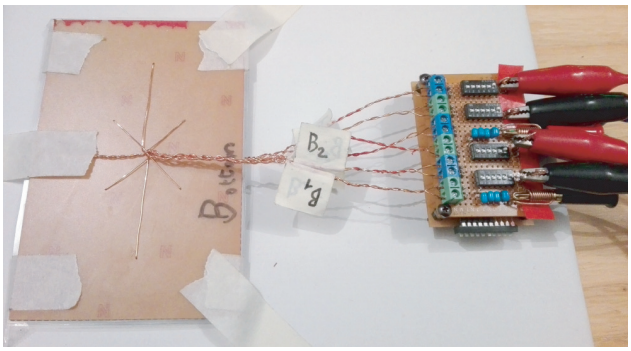

Figure 10. View of the PCB array experimental setup. On the left the Device Under Test (DUT), on the right the board used for routing power to the desired antenna and signal to the oscilloscope's inputs. Equivalent circuitry achieved with this board is depicted Fig. 9.

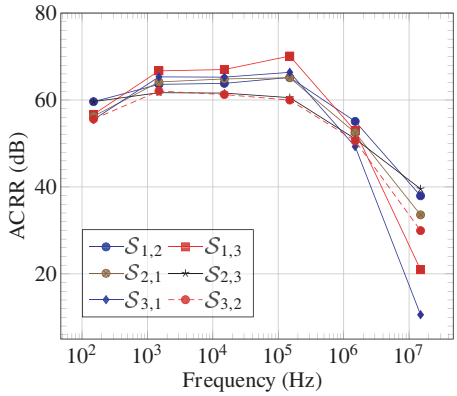

Figure 11. ACRR of PCB array calculated from experiment data at different frequencies.

4.1.4. Results

Net electric power P_j received by the $294.4\,\Omega + R_j$ load of an antenna ζ_j is accessible via the electric current matrices $[\mathbf{I\zeta}]$ (Cf. Table A9 to Table A14 in Appendix A) by the relation $P_j = (294.4 + R_j){I\zeta_j}^2$. Assuming that crosstalk is globally low between every channels, which is apparently the case up to 1.5 MHz, then $\mathcal{S}_{i,j} \simeq 20\log_{10}((294.4 + R_i)I\zeta_i/((294.4 + R_j)I\zeta_j)$, where ζ_i is the antenna connected to the power source, gives a good estimation of the ACRR. Results show a typical channel selectivity of 55 dB to 70 dB from 150 Hz to 150 kHz (Cf. Fig. 11).

The inductance matrices were automatically computed using an octave script proceeding in the following manner:

- the amplitude and phase of the sinusoidal signals $\Delta\alpha\beta$ and $\Delta\gamma\delta$ were determined by fitting an ideal sinusoid to the raw signal using a bisection method with threshold of $1 \times 10^{-5^\circ}$ on phase angle, 5×10^{-5} V on peak-to-peak amplitude and 1×10^{-5} V on common mode.
- this information and the measured ESR of each antenna (Cf. Appendix A Table A1) were injected into Equation (46).

Results are presented in Tables A15 to A20 of Appendix A.

4.2. 2 Channels Rotary Pie-Chart Array

The presented geometry was designed to address the main drawback of the "Circle" geometry proposed by Bieler et al. in [3]: a sensible level of interferences, even for the optimized "Circle" geometry tested in [7]. Unfortunately this last paper does not provide enough details to estimate the ACRR of Bieler

et al.'s model. Our particular version is a basic rotary type of 2 channels Pie-Chart array designed to improve ACRR of rotating type of Near Field Wireless Transmission of Power and Information device (NFWTPI).

4.2.1. Design and Manufacture

From a time perspective, the rotary prototype was built and tested prior to the PCB one. At that time, primary design constraint was the availability of tools and materials. As a simple proof of concept, we came out with the design depicted Fig. 12. Device was built using 48 mm inside/outside diameter PVC tube, of 0.35 mm core diameter insulated copper wire and a drill press. In this case, "power" channel $\{P_{in}, P_{out}\}$ was designed with a higher self inductance than the "data" channel $\{D_{in}, D_{out}\}$.

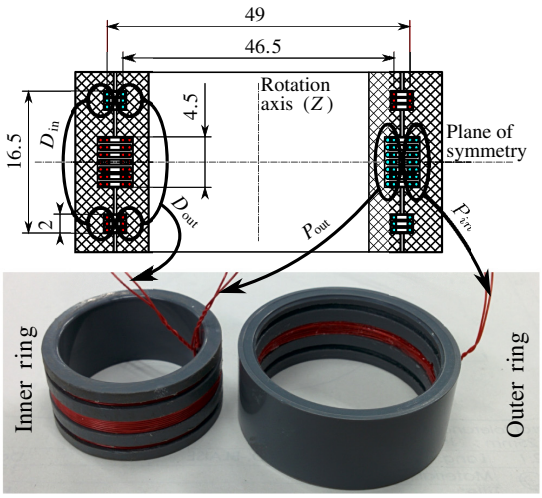

(a)

(μH)	$M_{P_{in},j}$	$M_{D_{in},j}$	$M_{P_{out},j}$	$M_{D_{out},j}$
$M_{i,P_{in}}$	19.1016	0.0006	14.1235	0.0004
$M_{i,D_{in}}$	0.0006	1.8618	0.0004	0.9639
$M_{i,P_{out}}$	14.1235	0.0004	17.2306	0.0005
$M_{i,D_{out}}$	0.0004	0.9639	0.0005	1.6974

(b)

Figure 12. (a) Construction of the non-contact slip ring's, or rotary array, and (b) associated inductance matrix numerically evaluated. Red and blue colors on the top cross-section differentiate the orientation of electric current inside the coils conductors. Coils P_{in} and P_{out} are each made of 14 turns of conductor, D_{in} and D_{out} are each made of 2×3 turns of conductor.

4.2.2. Results

Numerical results presented in the table of Fig. 12 were obtained using the same methodology as that of the PCB array. Based on this table, we can expect a minimum ACRR $\mathcal{S}_{P,D}$ close to 91 dB and $\mathcal{S}_{D,P}$ close to 67 dB. Once again we present, in Fig. 13, the expected evolution of ACRR $\mathcal{S}_{i,j}$ function of misalignment along the rotation axis (Z axis). Fig. 14 shows the ACRR evaluated from the experimental results. Evaluated inductance matrices presented in Tables A21 to A26 of Appendix A were obtained using a similar procedure to that of the PCB array. The measured ESR used in those calculations are presented in Table A2 of Appendix A, and the currents through the inductors are presented in Table A3 to A8.

5. DISCUSSION

Experimental results globally agree with the theory: we observe a significant ACRR in most of the tested configurations. However, there are several discrepancies that we will discuss in this section.

5.1. Symmetry of the Inductance Matrices

Up to Neumann formula, the inductance matrices should be symmetric. Let's define a coefficient W which qualifies how symmetric is a given square matrix $[\mathbf{M}]$ of size n. W is equal to 1 minus the average

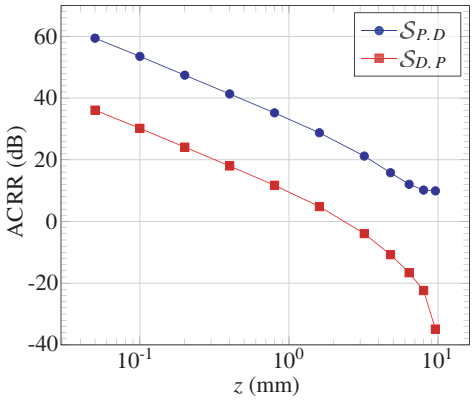

Figure 13. Numerically evaluated impact of the rotary array misalignment along the z axis on the ACRR.

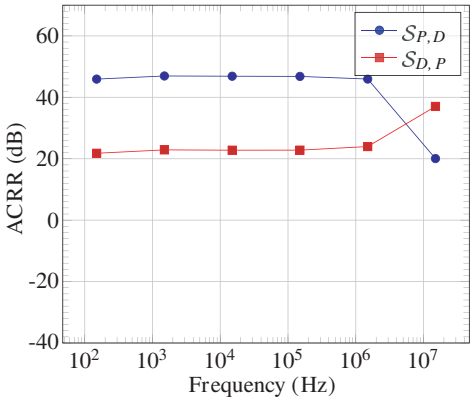

Figure 14. ACRR of rotary array calculated from experiment data at different frequencies.

ratio of the difference between two diagonally opposed terms over the range of all non-diagonal terms such as:

$$W = 1 - \frac{2}{n^2 - n} \sum_{i=2}^{n} \sum_{j=1}^{i-1} \frac{|M_{i,j} - M_{j,i}|}{\max(M^*) - \min(M^*)} \tag{47}$$

where $M_{i,j}$ is the term at the ith line jth column of $[\mathbf{M}]$, and M^* are all the non-diagonal terms of $[\mathbf{M}]$. Note that we consider only the real part of each term. The W factors for inductance matrices presented in Tables A15 to A26 all exceed 99%. In comparison, the expected W factor is about $60.6\%^{+10.2\%}_{-10.6\%}$ for a random 4×4 matrix and $64.4\%^{+6.1\%}_{-6.4\%}$ for a 6×6 one. Model and experiments are consistent on this point.

5.2. Inductance

Based on Lenz's Law, the self inductance of a simple conductor is always positive. At 15 MHz both PCB and rotary array's self-inductance are negative (Cf. diagonal terms of the inductance matrices Tables A15 to A26). On the other hand, we can observe an unusually large imaginary part at low frequency.

Stray capacitance may intuitively explain the negative self-inductance at high frequency. On the large imaginary part issue, we must acknowledge that an inductance's imaginary part is homogeneous to the real part of a complex impedance, i.e., a resistance. Indeed, the issue lies in the poor conditioning of the matrix $[\mathbf{M}]$ with respect to the ESR matrix $[\mathbf{R}]$ at low frequency.

Using a SPICE program to simulate the behavior of a simplified version of the PCB array experimental setup (Cf. Fig. 15), we observed that the $\pm 0.01\,\Omega$ measurement tolerance on $[\mathbf{R}]$ corresponded to about $\pm 10\,\mu$H deviation on the calculated self-inductance's imaginary part. In the mean time, we also noticed that even 90 pF per probe + oscilloscope input capacitance (very conservative value considering that we used straight 1.2 m unterminated lossless coaxial cables) is enough to significantly bias the calculated value of $[\mathbf{M}]$ above 3 MHz (Cf. Fig. 16). Hence the negative values were obtained at 15 MHz.

Notice that however a negative self-inductance might be alarming, and negative mutual inductance is not. The observed negative co-channel mutual inductance $M_{B2,T2}$ is consistent over the whole test frequency range. Indeed, this simply denotes that either ζ_{B2} or ζ_{T2} was plugged in reverse polarity.

5.3. Coupling and Selectivity

In the numerical analysis of Section 4.1.2, we would expect the ACRR of the PCB array to tend to infinity at position $(0, 0, 0.5)_{O;\hat{\mathbf{i}},\hat{\mathbf{j}},\hat{\mathbf{K}}}$ between channels. Instead we observed filtering capabilities globally

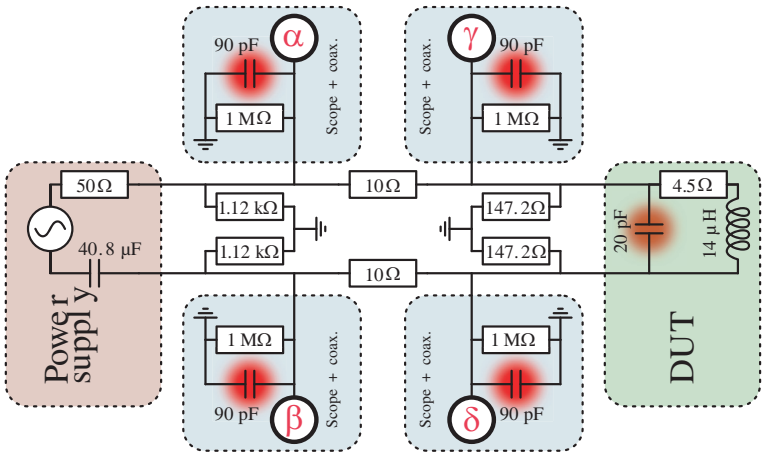

Figure 15. Schematic of the portion of the tested circuit simulated with the software ngspice-26. Parasitic capacitance are highlighted with blurry red dots. Scope inputs α, β, γ and δ are that presented in Fig. 9. Results of the simulation are presented Fig. 6.

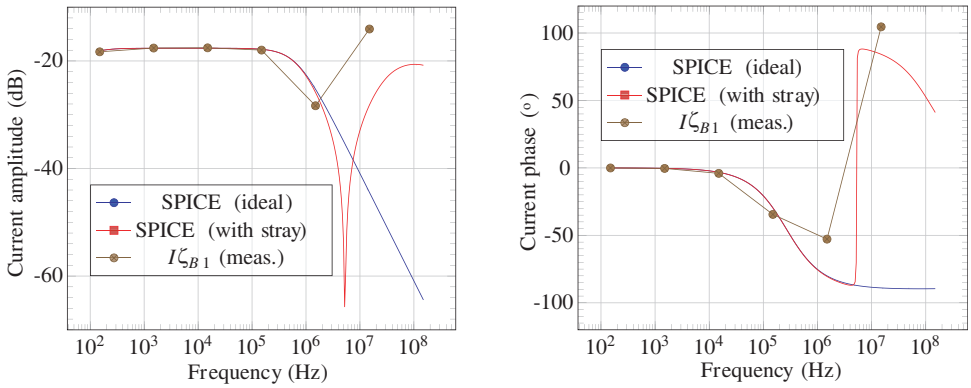

Figure 16. Comparison of the signal $(294.4 \times \Delta\alpha\beta - 314.4\Delta\gamma\delta)/5888$ between the simulated circuit Fig. 15 and the real antenna ζ_{B1}. The result allows to estimate the resonance frequency, above which the capacitive impedance will dominate over the inductance of a 14 µF antenna, thus leading to wrong calculation of the self inductance with our method (negative values). This is put in perspective with an ideal situation where the circuit would not contain parasitic capacitance. Their is not enough measurement points to precisely determine the resonance frequency of the real device. However, the curve obtained from simulation fits well enough the measurements to conclude that at 15 MHz the system definitely operates above its resonance frequency.

lower than 100 dB at that position. Furthermore, the highest filtering position varies from channel to channel.

Indeed, unlike the simple loop geometry used in example 2.3, the spiral geometry used here is not perfectly symmetric. To a smaller extend, this might be due to the numerical bias introduced by numerical round-off and the limited resolution of the numerical model.

The ACRR of the experimental rotary array is substantial over the whole tested frequency range: above 20 dB. However, it is about 3 orders of magnitude lower than the expected values from numerical evaluation.

It is reasonable to think that this high discrepancy is mainly due to the relatively poor building accuracy of the experimental device (machined with a drill press) and of the acquisition system. As can be seen in Fig. 13, a misalignment of only 0.1 mm could account for this difference. This might be further

emphasize by the low number of turns (higher sensitivity to random error) and by the compactness of the system in comparison to the PCB array.

Based on its definition (Equations (43) and (42)), ACRR's should be independent of the operating frequency. For both experimental devices, the calculated absolute ratio between co-channel and cross-channel couplings is higher than 10 (20 dB of ACRR) up to 1.5 MHz. Above that frequency, the ratio collapses to as low as 1.7 (about 5 dB). This phenomenon was not predicted by the presented Pie-Chart antenna model.

It is tempting to think that this is another consequence of the stray mutual capacitance between channels. Yet, given how randomly affected each ACRR seemed to be (at 15 MHz $\mathcal{S}_{3,1} \simeq 10\,\text{dB}$ whereas $\mathcal{S}_{2,3} \simeq 40\,\text{dB}$) we would expect an equally random capacitive coupling matrix for the system. Considering how similar we tried to make each antenna of the PCB device (similar self-inductance, similar total wire length hence the similar antenna ESR seen in Table A1, similar copper trace surface area) and the fact that each pair of wires was twisted, we would not expect the capacitance matrix of the system to be random. Similarly, explaining the sudden increase of $\mathcal{S}_{D,P}$ of the rotary array might be a not-so-obvious task.

Recent tests performed on the routing circuit visible in Fig. 10 indicated a sensible amount of noise from this circuit above 1 MHz. This might be further emphasized by the fact that this operating frequency is close to the resonance frequency of this circuit when being connected to a $10\,\mu\text{F} \sim 20\,\mu\text{F}$ antenna. We do not know yet how much this routing circuit noise accounts for the complete noise signal. A more careful design of the experimental setup to minimize the amount of stray capacitance from the measurement tools and routing circuit, as well as more detailled frequency domains response of the system may help to better characterize those phenomenons. We are currently investigating those issues and will hopefully provide our results in a later manuscript in preparation: "*Eliminate Crosstalk using Symmetry in MIMO Arrays of Inductive Antenna: Miscellaneous Properties of Pie-Chart Antennas.*".

6. CONCLUSION

A specific topology of multichannel inductive array of antennas was presented. It was shown to be theoretically efficient in filtering crosstalk. That was experimentally confirmed over a $150\,\text{Hz} \sim 1.5\,\text{MHz}$ frequency range. Building process, based on iterative symmetries, allows for very quick and cheap yet efficient design and manufacturing of multichannel device. This design simplicity was especially exemplified with the quick building and test of the 2 channels rotary type of inductive transmission device (wireless "slip ring").

Yet, we were unable to prove the effectiveness of the concept above this frequency range because of a too high amount of stray capacitance in the test system and because of an unexpected incoherent drop of ACRR at high frequency. Further investigations on those issues are currently carried out for a more complete understanding of the physics at play.

ACKNOWLEDGMENT

This research was financially supported by the Department of Education of the "Collectivité Territoriale de Martinique".

APPENDIX A. TABLES

Table A1. Calculated and measured Equivalent Series Resistance R_i (PCB array).

	R_{B1}	R_{B2}	R_{B3}	R_{T1}	R_{T2}	R_{T3}
Calculated (Ω)	4.38	4.81	5.13	4.38	4.81	5.13
Measured (Ω)	4.48	4.77	5.01	4.67	4.72	5.03
Error (%)	2.5	0.7	2.4	6.6	1.7	1.9

Table A2. Calculated and measured Equivalent Series Resistance R_i (rotary array).

	R_{Pin}	R_{Din}	R_{Pout}	R_{Dout}
Calculated (Ω)	0.50	0.22	0.46	0.20
Measured (Ω)	0.52	0.16	0.45	0.23
Error (%)	3	28	3	13

Table A3. Current through the inductors evaluated at 150 Hz (rotary array).

(mA)	XP_1	XP_2	XP_3	XP_4
$I\zeta_{Pin}$	129.12 $-0.05°$	0.00 $64.95°$	0.01 $-90.13°$	0.00 $131.20°$
$I\zeta_{Din}$	0.00 $87.32°$	129.82 $-0.01°$	0.00 $84.04°$	0.00 $90.55°$
$I\zeta_{Pout}$	0.01 $-90.14°$	0.00 $96.99°$	129.22 $-0.05°$	0.00 $-71.59°$
$I\zeta_{Dout}$	0.00 $-60.46°$	0.00 $89.37°$	0.00 $-78.92°$	129.71 $-0.00°$

Table A4. Current through the inductors evaluated at 1.5 kHz (rotary array).

(mA)	XP_1	XP_2	XP_3	XP_4
$I\zeta_{Pin}$	140.70 $-0.53°$	0.00 $88.43°$	0.06 $-90.62°$	0.00 $-139.11°$
$I\zeta_{Din}$	0.00 $87.41°$	141.63 $-0.06°$	0.00 $88.48°$	0.00 $89.85°$
$I\zeta_{Pout}$	0.06 $-90.67°$	0.00 $91.15°$	140.91 $-0.48°$	0.00 $-90.02°$
$I\zeta_{Dout}$	0.00 $-88.52°$	0.00 $89.73°$	0.00 $-90.41°$	141.44 $-0.05°$

Table A5. Current through the inductors evaluated at 15 kHz (rotary array).

(mA)	XP_1	XP_2	XP_3	XP_4
$I\zeta_{Pin}$	141.29 $-5.33°$	0.00 $89.48°$	0.61 $-95.28°$	0.00 $166.05°$
$I\zeta_{Din}$	0.00 $84.47°$	142.25 $-0.56°$	0.00 $84.82°$	0.04 $89.35°$
$I\zeta_{Pout}$	0.61 $-95.74°$	0.00 $89.19°$	141.43 $-4.85°$	0.00 $-91.29°$
$I\zeta_{Dout}$	0.00 $80.15°$	0.04 $89.32°$	0.00 $-94.23°$	142.05 $-0.53°$

Table A6. Current through the inductors evaluated at 150 kHz (rotary array).

(mA)	XP_1	XP_2	XP_3	XP_4
$I\zeta_{Pin}$	133.35 $-41.55°$	0.01 $77.03°$	5.79 $-133.17°$	0.00 $174.37°$
$I\zeta_{Din}$	0.01 $44.62°$	141.31 $-5.52°$	0.03 $48.92°$	0.38 $83.84°$
$I\zeta_{Pout}$	5.75 $-135.47°$	0.03 $79.98°$	134.46 $-39.01°$	0.02 $-100.01°$
$I\zeta_{Dout}$	0.00 $124.15°$	0.38 $83.55°$	0.01 $-130.52°$	141.13 $-5.18°$

Table A7. Current through the inductors evaluated at 1.5 MHz (rotary array).

(mA)	XP_1	XP_2	XP_3	XP_4
$I\zeta_{Pin}$	37.77 $-59.39°$	0.10 $-15.46°$	18.30 $171.32°$	0.08 $95.55°$
$I\zeta_{Din}$	0.04 $-4.43°$	133.47 $-41.80°$	0.09 $12.73°$	3.58 $44.29°$
$I\zeta_{Pout}$	17.12 $172.33°$	0.23 $15.00°$	41.59 $-58.09°$	0.14 $-173.44°$
$I\zeta_{Dout}$	0.03 $96.83°$	3.57 $43.00°$	0.06 $-173.03°$	134.14 $-40.02°$

Table A8. Current through the inductors evaluated at 15 MHz (rotary array).

(mA)	XP_1	XP_2	XP_3	XP_4
$I\zeta_{Pin}$	198.55 $109.43°$	0.11 $104.76°$	3.21 $17.84°$	0.15 $-24.53°$
$I\zeta_{Din}$	0.18 $99.15°$	126.64 $118.17°$	0.32 $-178.64°$	15.89 $-140.40°$
$I\zeta_{Pout}$	3.19 $18.22°$	0.24 $-179.13°$	188.70 $106.11°$	0.40 $15.19°$
$I\zeta_{Dout}$	0.30 $-2.90°$	17.19 $-137.41°$	0.74 $25.57°$	115.89 $115.65°$

Table A9. Current through the inductors evaluated at 150 Hz (PCB array).

(mA)	XP_1	XP_2	XP_3	XP_4	XP_5	XP_6
$I\zeta_{B1}$	121.66 $-0.04°$	0.00 $67.99°$	0.00 $-134.34°$	0.01 $-90.10°$	0.00 $29.72°$	0.00 $3.64°$
$I\zeta_{B2}$	0.00 $31.01°$	121.07 $-0.04°$	0.00 $175.45°$	0.00 $25.98°$	0.01 $89.88°$	0.00 $-90.19°$
$I\zeta_{B3}$	0.00 $-23.31°$	0.00 $113.23°$	120.65 $-0.04°$	0.00 $14.07°$	0.00 $-46.67°$	0.01 $-90.08°$
$I\zeta_{T1}$	0.01 $-90.08°$	0.00 $83.31°$	0.00 $94.08°$	121.23 $-0.04°$	0.00 $68.65°$	0.00 $63.99°$
$I\zeta_{T2}$	0.00 $105.42°$	0.01 $89.94°$	0.00 $-96.83°$	0.00 $171.64°$	121.17 $-0.04°$	0.00 $-172.91°$
$I\zeta_{T3}$	0.00 $40.67°$	0.00 $-126.74°$	0.01 $-90.05°$	0.00 $64.59°$	0.00 $-22.46°$	120.57 $-0.04°$

Table A10. Current through the inductors evaluated at 1.5 kHz (PCB array).

(mA)	XP_1	XP_2	XP_3	XP_4	XP_5	XP_6
$I\zeta_{B1}$	131.83 $-0.38°$	0.00 $85.74°$	0.00 $86.10°$	0.06 $-90.52°$	0.00 $84.50°$	0.00 $83.55°$
$I\zeta_{B2}$	0.00 $91.49°$	131.18 $-0.38°$	0.00 $92.85°$	0.00 $86.85°$	0.06 $89.46°$	0.00 $-99.30°$
$I\zeta_{B3}$	0.00 $83.11°$	0.00 $77.45°$	130.62 $-0.38°$	0.00 $87.63°$	0.00 $-91.89°$	0.06 $-90.53°$
$I\zeta_{T1}$	0.06 $-90.54°$	0.00 $88.76°$	0.00 $95.11°$	131.36 $-0.38°$	0.00 $77.99°$	0.00 $80.66°$
$I\zeta_{T2}$	0.00 $90.54°$	0.06 $89.46°$	0.00 $-89.31°$	0.00 $90.95°$	131.22 $-0.38°$	0.00 $-123.75°$
$I\zeta_{T3}$	0.00 $85.50°$	0.00 $-92.06°$	0.06 $-90.54°$	0.00 $86.03°$	0.00 $-146.17°$	130.58 $-0.38°$

Table A11. Current through the inductors evaluated at 15 kHz (PCB array).

(mA)	XP_1	XP_2	XP_3	XP_4	XP_5	XP_6
$I\zeta_{B1}$	132.41 $-4.03°$	0.00 $85.08°$	0.00 $84.29°$	0.61 $-94.45°$	0.00 $87.22°$	0.00 $84.17°$
$I\zeta_{B2}$	0.00 $82.52°$	131.75 $-4.03°$	0.00 $79.27°$	0.00 $82.46°$	0.60 $85.50°$	0.00 $-92.24°$
$I\zeta_{B3}$	0.00 $76.24°$	0.00 $81.22°$	131.21 $-3.99°$	0.00 $80.05°$	0.00 $-93.24°$	0.58 $-94.47°$
$I\zeta_{T1}$	0.61 $-94.48°$	0.00 $85.36°$	0.00 $84.04°$	131.92 $-4.00°$	0.00 $85.75°$	0.00 $83.37°$
$I\zeta_{T2}$	0.00 $80.82°$	0.60 $85.51°$	0.00 $-92.56°$	0.00 $79.98°$	131.78 $-4.03°$	0.00 $-82.99°$
$I\zeta_{T3}$	0.00 $78.87°$	0.00 $-91.57°$	0.58 $-94.47°$	0.00 $80.69°$	0.00 $-82.39°$	131.10 $-3.98°$

Table A12. Current through the inductors evaluated at 150 kHz (PCB array).

(mA)	XP_1	XP_2	XP_3	XP_4	XP_5	XP_6
$I\zeta_{B1}$	126.18 $-34.47°$	0.00 $50.76°$	0.00 $60.41°$	5.77 $-128.19°$	0.00 $61.81°$	0.00 $52.90°$
$I\zeta_{B2}$	0.00 $55.99°$	125.40 $-34.48°$	0.00 $50.68°$	0.00 $55.77°$	5.75 $51.45°$	0.00 $-130.58°$
$I\zeta_{B3}$	0.00 $65.73°$	0.00 $53.39°$	124.92 $-34.23°$	0.00 $49.34°$	0.01 $-131.49°$	5.47 $-128.32°$
$I\zeta_{T1}$	5.72 $-128.39°$	0.00 $58.87°$	0.00 $63.55°$	125.71 $-34.27°$	0.00 $83.34°$	0.00 $57.68°$
$I\zeta_{T2}$	0.00 $57.63°$	5.69 $51.51°$	0.01 $-131.57°$	0.00 $59.52°$	125.45 $-34.48°$	0.00 $-141.09°$
$I\zeta_{T3}$	0.00 $50.75°$	0.00 $-130.01°$	5.47 $-128.38°$	0.00 $49.21°$	0.00 $-141.29°$	124.86 $-34.10°$

Table A13. Current through the inductors evaluated at 1.5 MHz (PCB array).

(mA)	XP_1	XP_2	XP_3	XP_4	XP_5	XP_6
$I\zeta_{B1}$	38.34 $-52.80°$	0.11 $-58.33°$	0.03 $-38.38°$	18.70 $175.88°$	0.04 $88.63°$	0.02 $11.29°$
$I\zeta_{B2}$	0.03 $90.52°$	38.21 $-52.84°$	0.02 $104.15°$	0.03 $85.94°$	18.51 $-4.76°$	0.05 $124.61°$
$I\zeta_{B3}$	0.03 $102.30°$	0.03 $108.77°$	39.29 $-55.74°$	0.03 $86.78°$	0.04 $130.94°$	17.93 $174.06°$
$I\zeta_{T1}$	18.75 $175.83°$	0.01 $42.26°$	0.06 $103.37°$	38.21 $-52.82°$	0.16 $109.62°$	0.08 $103.78°$
$I\zeta_{T2}$	0.03 $101.83°$	18.43 $-4.73°$	0.05 $122.09°$	0.04 $104.32°$	38.50 $-52.56°$	0.03 $109.32°$
$I\zeta_{T3}$	0.04 $108.18°$	0.05 $127.96°$	17.82 $174.06°$	0.04 $101.02°$	0.04 $112.68°$	39.25 $-54.54°$

Table A14. Current through the inductors evaluated at 15 MHz (PCB array).

(mA)	XP_1	XP_2	XP_3	XP_4	XP_5	XP_6
$I\zeta_{B1}$	198.25 $104.56°$	0.07 $92.68°$	0.31 $138.54°$	6.02 $13.80°$	0.09 $8.76°$	0.57 $6.10°$
$I\zeta_{B2}$	0.08 $66.82°$	183.01 $104.31°$	0.10 $8.02°$	0.08 $76.93°$	5.87 $-164.94°$	0.06 $57.71°$
$I\zeta_{B3}$	0.37 $140.20°$	0.03 $23.34°$	194.39 $104.98°$	0.54 $172.09°$	0.06 $52.31°$	1.97 $23.38°$
$I\zeta_{T1}$	6.01 $15.39°$	0.12 $112.53°$	0.56 $175.93°$	186.25 $101.77°$	0.12 $35.02°$	0.31 $11.85°$
$I\zeta_{T2}$	0.07 $40.07°$	5.53 $-163.50°$	0.06 $77.61°$	0.08 $37.55°$	198.82 $101.71°$	0.07 $122.07°$
$I\zeta_{T3}$	0.47 $1.79°$	0.06 $49.38°$	1.90 $23.86°$	0.35 $1.00°$	0.07 $141.85°$	206.94 $103.98°$

Table A15. Evaluated PCB array's inductance matrix at 150 Hz[§].

(μH)	$M_{B1,j}$	$M_{B2,j}$	$M_{B3,j}$	$M_{T1,j}$	$M_{T2,j}$	$M_{T3,j}$
$M_{i,B1}$	$16.540_{-96.211j}$	$-0.010_{+0.004j}$	$0.003_{-0.003j}$	$14.283_{-0.016j}$	$-0.011_{+0.019j}$	$-0.001_{+0.015j}$
$M_{i,B2}$	$-0.004_{+0.007j}$	$17.119_{+39.142j}$	$-0.002_{-0.021j}$	$-0.002_{+0.004j}$	$-14.303_{+0.020j}$	$0.007_{-0.000j}$
$M_{i,B3}$	$0.001_{+0.003j}$	$-0.011_{-0.005j}$	$17.795_{+121.928j}$	$-0.005_{+0.020j}$	$0.009_{+0.009j}$	$13.835_{-0.010j}$
$M_{i,T1}$	$14.298_{-0.008j}$	$-0.014_{+0.002j}$	$-0.023_{-0.002j}$	$16.685_{-307.465j}$	$-0.008_{+0.003j}$	$-0.013_{+0.006j}$
$M_{i,T2}$	$-0.014_{-0.004j}$	$-14.299_{+0.005j}$	$0.023_{-0.003j}$	$-0.002_{-0.015j}$	$16.457_{+80.503j}$	$0.003_{-0.023j}$
$M_{i,T3}$	$-0.007_{+0.008j}$	$0.012_{-0.009j}$	$13.842_{-0.002j}$	$-0.013_{+0.006j}$	$0.008_{+0.019j}$	$16.440_{+89.336j}$

Table A16. Evaluated PCB array's inductance matrix at 1.5 kHz[§].

(μH)	$M_{B1,j}$	$M_{B2,j}$	$M_{B3,j}$	$M_{T1,j}$	$M_{T2,j}$	$M_{T3,j}$
$M_{i,B1}$	$16.499_{-9.046j}$	$-0.008_{+0.001j}$	$-0.003_{+0.000j}$	$14.559_{-0.029j}$	$-0.005_{+0.000j}$	$-0.008_{+0.001j}$
$M_{i,B2}$	$-0.010_{-0.000j}$	$16.659_{+4.786j}$	$-0.006_{-0.000j}$	$-0.010_{+0.000j}$	$-14.567_{+0.032j}$	$0.007_{-0.001j}$
$M_{i,B3}$	$-0.003_{+0.000j}$	$-0.005_{+0.001j}$	$16.635_{+13.168j}$	$-0.006_{+0.000j}$	$0.012_{-0.000j}$	$14.084_{-0.032j}$
$M_{i,T1}$	$14.558_{-0.033j}$	$-0.009_{+0.000j}$	$-0.006_{-0.001j}$	$16.430_{-29.744j}$	$-0.004_{+0.001j}$	$-0.008_{+0.001j}$
$M_{i,T2}$	$-0.008_{-0.000j}$	$-14.569_{+0.033j}$	$0.011_{+0.000j}$	$-0.006_{-0.000j}$	$16.619_{+9.185j}$	$0.001_{-0.001j}$
$M_{i,T3}$	$-0.007_{+0.000j}$	$0.009_{-0.000j}$	$14.089_{-0.031j}$	$-0.009_{+0.001j}$	$0.001_{-0.001j}$	$16.525_{+10.095j}$

Table A17. Evaluated PCB array's inductance matrix at 15 kHz[§].

(μH)	$M_{B1,j}$	$M_{B2,j}$	$M_{B3,j}$	$M_{T1,j}$	$M_{T2,j}$	$M_{T3,j}$
$M_{i,B1}$	$17.324_{-0.813j}$	$-0.009_{+0.000j}$	$-0.003_{+0.000j}$	$14.551_{-0.035j}$	$-0.006_{-0.000j}$	$-0.008_{+0.000j}$
$M_{i,B2}$	$-0.010_{+0.001j}$	$17.548_{+0.586j}$	$-0.004_{+0.000j}$	$-0.009_{+0.001j}$	$-14.562_{+0.038j}$	$0.008_{+0.000j}$
$M_{i,B3}$	$-0.004_{+0.001j}$	$-0.005_{+0.000j}$	$17.569_{+1.425j}$	$-0.006_{+0.001j}$	$0.012_{+0.000j}$	$14.082_{-0.043j}$
$M_{i,T1}$	$14.551_{-0.035j}$	$-0.008_{+0.000j}$	$-0.005_{+0.000j}$	$17.335_{-2.887j}$	$-0.005_{+0.000j}$	$-0.009_{+0.000j}$
$M_{i,T2}$	$-0.007_{+0.001j}$	$-14.559_{+0.037j}$	$0.012_{+0.000j}$	$-0.006_{+0.001j}$	$17.540_{+1.008j}$	$0.002_{+0.000j}$
$M_{i,T3}$	$-0.006_{+0.001j}$	$0.009_{+0.000j}$	$14.083_{-0.040j}$	$-0.008_{+0.001j}$	$0.002_{+0.000j}$	$17.519_{+1.094j}$

Table A18. Evaluated PCB array's inductance matrix at 150 kHz[§].

(μH)	$M_{B1,j}$	$M_{B2,j}$	$M_{B3,j}$	$M_{T1,j}$	$M_{T2,j}$	$M_{T3,j}$
$M_{i,B1}$	$17.534_{-0.289j}$	$-0.009_{+0.000j}$	$-0.003_{-0.001j}$	$14.578_{-0.192j}$	$-0.006_{-0.001j}$	$-0.007_{-0.000j}$
$M_{i,B2}$	$-0.008_{-0.001j}$	$17.776_{-0.168j}$	$-0.003_{-0.000j}$	$-0.008_{-0.001j}$	$-14.581_{+0.221j}$	$0.009_{-0.001j}$
$M_{i,B3}$	$-0.002_{-0.001j}$	$-0.003_{-0.000j}$	$17.776_{-0.128j}$	$-0.004_{-0.000j}$	$0.014_{-0.001j}$	$13.936_{-0.248j}$
$M_{i,T1}$	$14.418_{-0.188j}$	$-0.008_{-0.001j}$	$-0.004_{-0.001j}$	$17.556_{-0.509j}$	$-0.003_{-0.002j}$	$-0.007_{-0.001j}$
$M_{i,T2}$	$-0.005_{-0.000j}$	$-14.421_{+0.204j}$	$0.014_{-0.001j}$	$-0.004_{-0.000j}$	$17.759_{-0.152j}$	$0.003_{-0.001j}$
$M_{i,T3}$	$-0.004_{-0.000j}$	$0.011_{-0.001j}$	$13.937_{-0.233j}$	$-0.007_{-0.000j}$	$0.003_{-0.001j}$	$17.724_{-0.181j}$

Table A19. Evaluated PCB array's inductance matrix at 1.5 MHz[§].

(μH)	$M_{B1,j}$	$M_{B2,j}$	$M_{B3,j}$	$M_{T1,j}$	$M_{T2,j}$	$M_{T3,j}$
$M_{i,B1}$	$22.917_{-2.770j}$	$-0.124_{+0.074j}$	$0.015_{+0.008j}$	$20.072_{-2.707j}$	$0.136_{-0.062j}$	$0.022_{-0.016j}$
$M_{i,B2}$	$-0.007_{-0.041j}$	$22.876_{-3.062j}$	$-0.001_{-0.021j}$	$-0.008_{-0.034j}$	$-19.783_{+3.095j}$	$0.019_{-0.042j}$
$M_{i,B3}$	$0.049_{-0.041j}$	$0.014_{-0.035j}$	$21.938_{-2.536j}$	$0.042_{-0.033j}$	$0.023_{-0.033j}$	$18.388_{-2.851j}$
$M_{i,T1}$	$20.025_{-2.743j}$	$-0.149_{+0.008j}$	$0.049_{-0.076j}$	$22.846_{-2.731j}$	$0.112_{-0.128j}$	$0.054_{-0.099j}$
$M_{i,T2}$	$0.010_{-0.030j}$	$-19.883_{+3.039j}$	$0.034_{-0.048j}$	$0.013_{-0.036j}$	$22.829_{-3.138j}$	$0.013_{-0.030j}$
$M_{i,T3}$	$0.057_{-0.050j}$	$0.029_{-0.043j}$	$18.448_{-2.572j}$	$0.049_{-0.045j}$	$0.006_{-0.038j}$	$21.921_{-2.942j}$

Table A20. Evaluated PCB array's inductance matrix at 15 MHz[§].

(μH)	$M_{B1,j}$	$M_{B2,j}$	$M_{B3,j}$	$M_{T1,j}$	$M_{T2,j}$	$M_{T3,j}$
$M_{i,B1}$	$-0.560_{+0.393j}$	$0.000_{+0.001j}$	$-0.002_{+0.004j}$	$0.090_{-0.015j}$	$0.001_{-0.000j}$	$0.007_{-0.002j}$
$M_{i,B2}$	$0.001_{+0.001j}$	$-0.609_{+0.408j}$	$0.001_{-0.000j}$	$0.001_{+0.001j}$	$-0.083_{+0.013j}$	$0.001_{+0.000j}$
$M_{i,B3}$	$-0.002_{+0.005j}$	$0.000_{-0.000j}$	$-0.571_{+0.406j}$	$-0.007_{+0.004j}$	$0.001_{+0.000j}$	$0.027_{-0.001j}$
$M_{i,T1}$	$0.085_{-0.017j}$	$0.000_{+0.002j}$	$-0.007_{+0.004j}$	$-0.602_{+0.374j}$	$0.002_{+0.000j}$	$0.004_{-0.001j}$
$M_{i,T2}$	$0.001_{+0.000j}$	$-0.085_{+0.014j}$	$0.000_{+0.001j}$	$0.001_{+0.000j}$	$-0.565_{+0.369j}$	$-0.000_{+0.001j}$
$M_{i,T3}$	$0.006_{-0.003j}$	$0.001_{+0.000j}$	$0.028_{-0.001j}$	$0.005_{-0.002j}$	$-0.000_{+0.001j}$	$-0.538_{+0.387j}$

Table A21. Evaluated rotary array's inductance matrix at 150 Hz[§].

$M_{i,Pin}$	18.811 -10.388_J	-0.027 $+0.013_J$	13.279 -0.017_J	-0.002 -0.002_J
$M_{i,Din}$	-0.033 $+0.002_J$	1.918 -9.111_J	-0.067 $+0.007_J$	-0.828 -0.008_J
$M_{i,Pout}$	13.280 -0.020_J	-0.066 -0.008_J	17.008 -10.514_J	0.029 $+0.010_J$
$M_{i,Dout}$	0.013 $+0.007_J$	-0.819 $+0.009_J$	0.034 $+0.007_J$	1.728 -11.318_J

Table A22. Evaluated rotary array's inductance matrix at 1.5 kHz[§].

(μH)	$M_{Pin,j}$	$M_{Din,j}$	$M_{Pout,j}$	$M_{Dout,j}$
$M_{i,Pin}$	18.945 -1.185_J	-0.027 $+0.001_J$	13.529 -0.024_J	0.001 -0.001_J
$M_{i,Din}$	-0.030 $+0.001_J$	1.930 -0.859_J	-0.061 $+0.001_J$	-0.826 $+0.001_J$
$M_{i,Pout}$	13.532 -0.025_J	-0.059 -0.001_J	17.050 -0.906_J	0.035 $+0.000_J$
$M_{i,Dout}$	0.014 $+0.001_J$	-0.826 $+0.003_J$	0.032 $+0.000_J$	1.792 -1.042_J

Table A23. Evaluated rotary array's inductance matrix at 15 kHz[§].

(μH)	$M_{Pin,j}$	$M_{Din,j}$	$M_{Pout,j}$	$M_{Dout,j}$
$M_{i,Pin}$	19.070 -0.179_J	-0.028 -0.000_J	13.524 -0.020_J	-0.000 -0.000_J
$M_{i,Din}$	-0.030 -0.000_J	1.973 -0.083_J	-0.061 $+0.000_J$	-0.835 $+0.001_J$
$M_{i,Pout}$	13.524 -0.022_J	-0.061 -0.000_J	17.286 -0.164_J	0.035 -0.000_J
$M_{i,Dout}$	-0.001 $+0.000_J$	-0.835 $+0.001_J$	0.033 $+0.000_J$	1.855 -0.101_J

Table A24. Evaluated rotary array's inductance matrix at 150 kHz[§].

(μH)	$M_{Pin,j}$	$M_{Din,j}$	$M_{Pout,j}$	$M_{Dout,j}$
$M_{i,Pin}$	18.946 -0.328_J	-0.029 -0.001_J	13.512 -0.164_J	0.000 -0.000_J
$M_{i,Din}$	-0.030 -0.001_J	1.941 -0.040_J	-0.062 $+0.000_J$	-0.841 $+0.009_J$
$M_{i,Pout}$	13.510 -0.183_J	-0.061 $+0.000_J$	17.196 -0.240_J	0.036 -0.001_J
$M_{i,Dout}$	-0.000 $+0.000_J$	-0.842 $+0.009_J$	0.035 -0.001_J	1.826 -0.036_J

Table A25. Evaluated rotary array's inductance matrix at 1.5 MHz[§].

(μH)	$M_{Pin,j}$	$M_{Din,j}$	$M_{Pout,j}$	$M_{Dout,j}$
$M_{i,Pin}$	22.839 -2.335_J	-0.047 -0.008_J	17.774 -1.996_J	0.010 -0.010_J
$M_{i,Din}$	-0.049 -0.011_J	1.915 -0.113_J	-0.078 -0.002_J	-0.839 $+0.032_J$
$M_{i,Pout}$	17.689 -1.944_J	-0.080 -0.005_J	20.817 -2.016_J	0.047 -0.014_J
$M_{i,Dout}$	0.010 -0.007_J	-0.840 $+0.028_J$	0.046 -0.013_J	1.808 -0.116_J

Table A26. Evaluated rotary array's inductance matrix at 15 MHz[§].

(μH)	$M_{Pin,j}$	$M_{Din,j}$	$M_{Pout,j}$	$M_{Dout,j}$
$M_{i,Pin}$	-0.546 $+0.398_J$	0.001 $+0.002_J$	0.047 -0.008_J	0.002 -0.003_J
$M_{i,Din}$	0.001 $+0.002_J$	-0.782 $+0.662_J$	-0.004 $+0.001_J$	-0.354 $+0.023_J$
$M_{i,Pout}$	0.044 -0.010_J	-0.004 $+0.002_J$	-0.586 $+0.373_J$	0.009 -0.003_J
$M_{i,Dout}$	0.003 -0.003_J	-0.353 $+0.031_J$	0.010 -0.001_J	-0.868 $+0.662_J$

REFERENCES

1. Adamson, A. and A. Berdugo, "Helicopter slip ring replacement system," *International Telemetering Conference*, Oct. 2010.
2. Ebrahimi, K. M., A. Lewalski, A. Pezouvanis, and B. Mason, "Piston data telemetry in internal combustion engines," *American Journal of Sensor Technology*, Vol. 2, No. 1, 7–12, Jan. 2014.
3. Bieler, T., M. Perrottet, V. Nguyen, and Y. Perriard, "Contactless power and information transmission," *IEEE Trans. Industry Applications*, Vol. 38, No. 5, 1266–1272, Sept./Oct. 2002.

§ Notice that the real part is the actual inductance whereas the imaginary part is homogeneous to a resistance.

4. Rosa, E. B., "The self and mutual inductance of linear conductor," *Bul. of Bureau of Standard*, Vol. 4, No. 2, 301–344, 1908.
5. Sugar, G. L., C. Vaidyanathan, and Y. Tesfai, "System and method for antenna diversity using joint maximal ratio combining," *World International Property Organization*, Patent No. US 6 687 492 B1, Jun. 2002.
6. Stirling-Gallacher, R., "Multiple-input multiple output spatial multiplexing system with dynamic antenna beam combination selection capability," *World International Property Organization*, Patent No. US 8 369 436 B2, Feb. 2013.
7. Rathge, C. and D. Kuschner, "High efficient inductive energy and data transmission system with special coil geometry," *13th European Conference on Power Electronics and Applications*, Sept. 2009.
8. Porter, V. J., "Magnetic recording heads utilizing symmetrical windings to avoid cross talk," *World International Property Organization*, Patent No. 3 287 713, Nov. 1966.
9. Dorf, R. C., *The Electrical Engineering Handbook*, 2nd Edition, CRC press, Sept. 1997.
10. Harrison, R. R., "Designing efficient inductive power links for implantable devices," *IEEE International Symposium on Circuits and Systems*, May 2007.
11. Hirai, J., T.-W. Kim, and A. Kawamura, "Study on crosstalk in inductive transmission of power and information," *IEEE Trans. Industrial Electronics*, Vol. 46, No. 6, 1174–1182, Dec. 1999.
12. Kreyszig, E., *Advanced Engineering Mathematics*, 10th edition, Wiley, Aug. 2011.